Multi-objective performance assessment of HVAC systems and physical barriers on COVID-19 infection transmission in a high-speed train

Mahdi Ahmadzadeh, Mehrzad Shams[*]

Faculty of Mechanical Engineering, K.N.Toosi University of Technology, Pardis St., Vanak Sq., Tehran, Iran

ARTICLE INFO

ABSTRACT

A computational fluid dynamics (CFD) simulation was performed to model and study the transmission risk associated with cough-related SARS-CoV-2 droplets in a real-world high-speed train (HST). In this study, the evaporating of the droplets was considered. Simulation data were post-processed to assess the fraction of the particles deposited on each passenger's face and body, suspended in air, and escaped from exhausts. Firstly, the effects of temperature, relative humidity, ventilation rate, injection source, exhausts' location and capacity, and adding the physical barriers on evaporation and transport of respiratory droplets are investigated in long distance HST. The results demonstrate that overall, 6–43% of the particles were suspended in the cabin after 2.7 min, depending on conditions, and 3–58% of the particles were removed from the cabin in the same duration. Use of physical barriers and high ventilation rate is therefore recommended for both personal and social protection. We found more exhaust capacity and medium relative humidity to be effective in reducing the particles' transmission potential across all studied scenarios. The results indicate that reducing ventilation rate and exhaust capacity, increased aerosols shelf time and dispersion throughout the cabin.

List of nomenclature

Abbreviation

ACH	Air Change Per Hour
B.Cs	Boundary Conditions
CFD	Computational Fluid Dynamic
CRH	China Railway High-Speed
COVID-19	Corona Virus Disease-2019
DPM	Discrete Phase Model
DRW	Discrete Random Walk
HVAC	Heating, Ventilation, And Air Conditioning
LHSTC	Long High-Speed Train Cabin
PT	Public Transportation

---

* Corresponding author.
E-mail addresses: ahmadzadeh7637@yahoo.com (M. Ahmadzadeh), shams@kntu.ac.ir (M. Shams).

RANS   Reynolds-Averaged Navier-Stokes
RH   Relative Humidity
SARS   Severe Acute Respiratory Syndrome
SARS-CoV-2   Severe Acute Respiratory Syndrome Coronavirus 2
SIMPLE   Semi Explicit Method For Pressure Equations

Parameter

D_k	m^2/s	Kinematic diffusivity of water vapor in the air
d_p	m	Particle diameter
E	J	Energy
F_B	N	Brownian force
F_D	N	Drag force
F_G	N	Gravitational force
F_L	N	Lift force
g_i	m/s^2	The gravitation acceleration in the x_i Direction
J_i	$kg/m^2 s$	Diffusive flux of species i
k_B	J/K	Boltzman constant
L	m	Distance to the nearest wall
l	m	Turbulence length scale
m_{d0}	kg/s	Mass of the droplet
$\dot{m}_{d0}$	kg/s	Rate of change of droplet mass
Δm_d	kg/s	Change in droplet mass
m_p	kg	Particle mass
p	Pa	Pressure
r	m	Particle radius
T	K	Temperature
t	s	Time
V	m^3	Aerosol (also control) volume
ν_t	m^2/s	Turbulent viscosity
U	m/s	Local mean velocity
u_i	m/s	Flow velocity in the x_i Direction
$u_i^{'}$	m/s	Fluctuating eddy velocity
u_f	m/s	The velocity of the fluid at the aerosol location
u_p	m/s	Particle velocity
x	m	Fluid location
x_p	m	Particle location
C		One-equation eddy viscosity constant
C_c		Cunningham correction factor
C_D		Drag coefficient
C_μ		$k-\varepsilon$ model empirical constant
Kn		Knudsen number
Pr_t		turbulent Prandtl number
Re_d		Droplet Reynold's number
Sc_t		Turbulent Schmidt number
sgn		Sign function
Y		Specific mass fraction

Greek symbols

ρ	kg/m^3	Density
ρ_f	kg/m^3	Density of the fluid
ρ_P	kg/m^3	Particle density
μ_{eff}	$Pa.s$	Effective Viscosity
μ_f	$Pa.s$	Fluid dynamic viscosity coefficient
μ_t	$Pa.s$	Eddy viscosity
λ	m	Mean free path
λ_a	W/mK	Air thermal conductivity
λ_{eff}	W/mK	Effective thermal conductivity
λ_t	W/mK	Turbulent thermal conductivity
τ_{ij}	Pa	Reynolds stresses
ε	m^2/s^3	Turbulence dissipation rate

ν	m^2/s Fluid kinematic viscosity coefficient
π	Pi number (≈ 3.14)
ζ	Normal random number

Subscripts

| a	Air
d	Droplets
eff	Effective
in	Droplets entering a control volume
inj	Injection
lat	Latent
out	Droplets exiting a control volume
Ref	Reference
T	Total
vap	Vaporization

1. Introduction

The growth and development of societies, along with the well-being and comfort it brings, also carry with them some challenges, sometimes overtly and sometimes covertly. That various and new types of diseases are one of the undesirable consequences of human interventions in the world order. The outbreak of COVID-19, caused by the SARS-CoV-2 (severe acute respiratory syndrome coronavirus 2) virus, happened in late 2019 and within six months has been rapidly spreading worldwide, causing a public health and economics crisis [1]. During this epidemic, all human societies suffered from disorders in various areas of communication that affected society, the psyche, business, the economy, lifestyle, and especially the world order. Even after considerable progress in vaccination that has resulted in a reduction in new infections and mortality rates, there have been instances of recurrence of the pandemic still through new variants in various countries. Unfortunately, at the time of writing in February 2022, the COVID-19 pandemic has claimed more than 5.7 million lives with more than 400 million people known to be infected worldwide [2]. Many public transportation (PT) agencies have implemented safety measures, including observing social distancing by reducing the capacity of occupants and requiring passengers to wear masks. Therefore, assessing aerosol transmission and adopting effective and low-cost viable measures to mitigate the disease transmission in PT remains a pressing matter. Preliminary epidemiological and virological observations and studies discovered that the transmission of the SARS-CoV-2 virus is mainly through person-to-person contact, through droplets emitted by respiratory events such as coughing, sneezing, or talking occurs [3–5]. Subsequently, it was suggested that, in indoor and poorly ventilated environments, the predominant transmission route of infection is through aerosols (particles smaller than 5 μm of diameter) containing viable viral particles generated by contaminated people [6,8].

Experiments and computational fluid dynamics (CFD) methods are the robust tools commonly applied to investigate the airborne transmission of pathogens between indoor occupants. Experimental measurements are usually very expensive and time-consuming [9, 10]. Whereas, CFD is a powerful and low-cost approach to counteracting the spread and transmission of viral diseases [11]. Meanwhile, researchers have used computational modeling techniques to assess the potential effectiveness of non-pharmaceutical reduction strategies [12] for a wide range of indoor environments, such as: classroom [13,14], library [15], world-real train cabin [16], car parking [17], urban subway [18], and airplane [19]. As with many other confined spaces, the air quality for PT, such as train cabins, is a primary and vital determining factor for transmission of COVID-19.

The Eulerian and the Lagrangian approaches are broadly two methodologies to simulate the dispersion of aerosols in CFD [13, 20–22]. The researchers showed by comparing experimental data that both the Eulerian and Lagrangian approaches are suitable for modeling airborne particles [23,24]. In the Eulerian phase, the Reynolds-Averaged Navier Stokes Equations (RANS) with approximate turbulence schemes is commonly used to estimate the airflow field distribution within a computational domain and has been applied in many investigations relevant to COVID-19 transmission [25,26]. Coupling the Eulerian procedure with Lagrangian particle transport dynamics allows for the incorporation of the effects of aerosol particle's characterization into the simulations and enables accurate modeling of the physical forces that act on the aerosol particles due to gravity, drag, lift, and Brownian motion in the case of aerosol particles [13,14,27].

It is also worth noting that, according to research, the physical phenomena involved in the droplet transmission and spreading process are very complicated and challenging. In fact, the interaction of inertial and aerodynamic forces between the droplets and the air plays an important role in their propagation [28]. Nonetheless, it has been specified that the respiratory droplets and aerosols that are generated during respiratory events are the most probable route of SARS-CoV-2 virus transmission [29–31]. This observation is also proved for the SARS-CoV-2 virus in numerous relevant studies [3,32]. So that, the role of aerosols in the spreading and transmission of the SARS-CoV-2 virus is more important [6,33,34]. In the formed droplet cloud, the droplet diameter ranges from nano-sized to hundred microns, and they are present by maintaining a probability distribution [35–38]. The large-sized droplets, tend to sit on surfaces, while small droplets such as droplets about 10 μm tend to evaporate completely before settling [39]. Complete evaporation of small droplets leads to the formation of droplet nuclei called aerosols [40]. Aerosols, which are very small particles, stay in the air long enough (suspended) and increase the risk of exposure to infection [33].
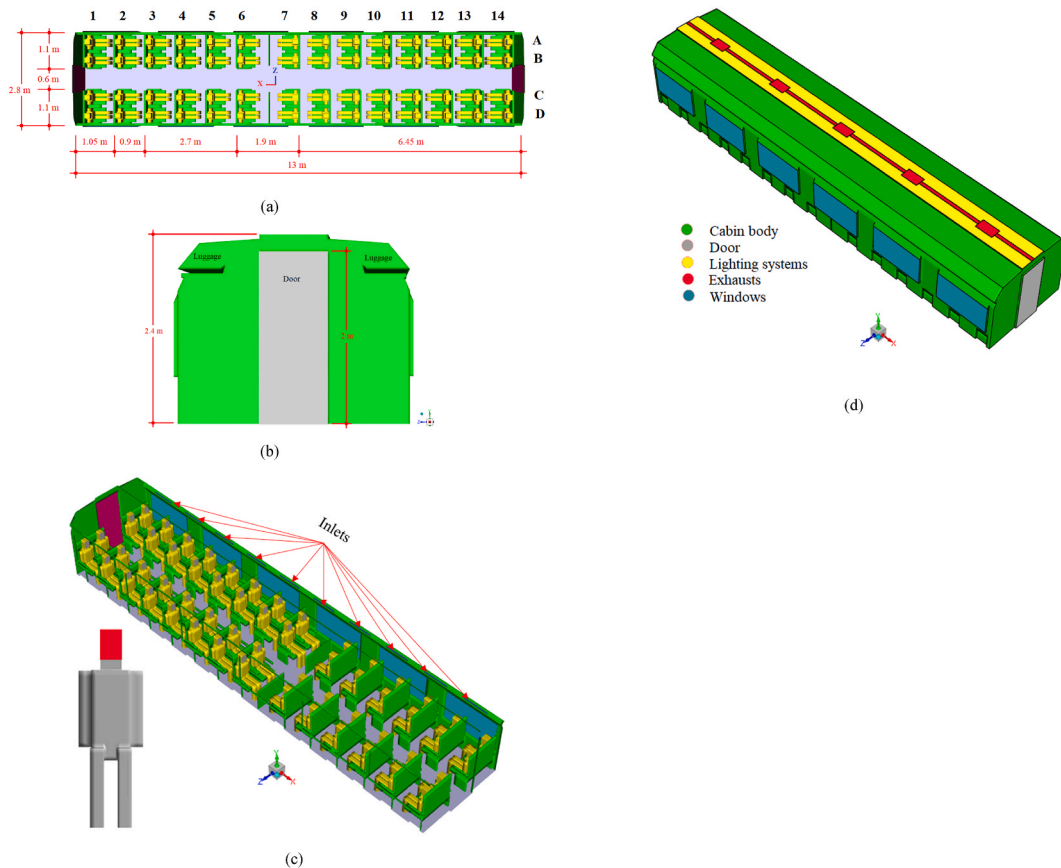
Fig. 1. Computational domain of a high-speed train (HST). (a) Passenger numbering and the dimensions of cabin on XZ plane, (b) dimensions of cabin on XY plane and luggage locations, (c) location of airflow inlets and the surface defined on the face (marked with a red area), and (d) locations of different parts of studied model. (For interpretation of the references to color in this figure legend, the reader is referred to the Web version of this article.)

One of the most important parameters in assessing the transmission of expelled droplets from respiratory events using CFD is the mass and heat exchange of droplets with the ambient environment [41]. Moreover, the mass of the droplet can vary due to evaporation, which is strictly connected to air temperature and relative humidity (RH). The existing scientific evidence demonstrated that wet climates reduce the spread of COVID-19 [42,43], due to the delay in evaporation time of the water content of the saliva droplets [39]. The physicochemical characteristics of evaporating droplets, under the effect of RH, were investigated by Ref. [44]. They find that physicochemical changes occurring in a droplet affect the efficiency of transmission of infectious disease by droplets and aerosols. Another important factor for the transmission of virions in the air is the evaporation of saliva droplets [41,45]. For more details of the generation, size, transmission, and etc. of saliva see Ref. [45] and references therein.

CFD models were developed by Wang et al. [46] to investigate the flow field, temperature field, and airflow pattern impacts on cough droplets dispersion processes in three different China railway high-speed (CRH) train cabins. They concluded that the air distribution system used in the China Railway High-Speed 5 (CRH5) model of the train cabin has the most efficient role in droplet removal among the three models studied. Analyzing the effects of four different diffuser types on ventilation and spread of diseases in HST cabins using CFD techniques, was employed by Yang et al. [47]. Simulation results indicated that selecting the diffuser type significantly affects overall cabin airflow pattern and particle contaminants transport. In the early stages of the COVID-19 pandemic, Ahmadzadeh and Shams [16] used CFD to investigate the effects of air conditioning, injection source, and exhaust flow location on the dispersion of talk-generate base aerosols inside a train cabin using the Eulerian-Lagrangian approach. The results revealed that opening the window remarkably reduces the aerosol shelf-time inside the domain. Talaat et al. [19] employed three passenger capacity-based models, including (a) a full passenger capacity, (b) a reduced capacity, and (c) a full capacity with sneeze guards/-shields between passengers, to study the aerosol transmission and intervention measures on a Boeing 737 cabin zone. The results demonstrated that the use of sneezing shields could be an appropriate alternative to full capacity flights instead of reducing passenger capacity. Furthermore, the effects of the ventilation rate, droplet size distribution, and physical partitions on the droplet spreading emitted by coughing of an infected teacher in front of a classroom were studied by Mirzaei et al. [14]. They found that the use of seat partitions, as well as increased ventilation, could prevent infection to some extent.

The current Covid-19 pandemic has revived the importance of using pandemic prevention operations, especially in indoor environments, as the prevalence rate is higher indoor environments. Preventive measures such as creating social distance, covering the

Table 1
Summary of continuous and dispersed phases boundary conditions.

Eulerian phase	Inlet	Velocity inlet; Various supply velocity: 0.1, 0.2, and 0.3 m/s; Various RH: 25, 50, and 75%; Various supply temperatures: 17, 20, *and* 25 °C; Turbulent intensity = 5%; Turbulent Length Scale = 0.035 m; Dimensions = 5 cm × 72 cm; Numbering = 20; Escape.
	Exhaust	Pressure outlet; Various exhaust temperature: 25, 27, and 18 °C; Escape.
	Wall	Windows: No-slip; 27 °C; Doors: No-slip; 25 °C; lighting: No-slip; 30 °C; Surfaces: No-slip; adiabatic; Passengers: No-slip; 25 °C; Passenger face: No-slip; 36 °C; All trap.
Lagrangian phase	Expiratory flow	Coughing; $v_{inj} = 11.2\,m/s$; Injection type: cone; Injection angle = 30.
	Composition [62]	98.2% Water + 1.8% Saliva; density = 1000 kg/m^3
	Diameter (μm)	(2, 4, 8, 16, 24, 32, 40, 75, 100)
	Duration (t)	$t = 0.5\,s$;
	particles (n)	$n = 4900$
	Simulation configuration	Time step $= \begin{cases} 0.005\,s, & 0 \le t < 10 \\ 0.05\,s & t \ge 10 \end{cases}$
		Overall simulation time: 210 s

face, quarantine and vaccination require enormous social, medical, psychological and economic costs, even as the emergence of different types of virus variants continues to be a concern. Therefore, it is vital to adopt appropriate strategies to reduce the transmission of SARS-CoV-2 indoors and outdoors to reduce the number of COVID-19 cases.

The knowledge of combined HVAC and geometry optimization effects on SARS-CoV-2 and other virus survival and transmission in the indoor environment is limited. This study numerically investigates the prediction of COVID-19 exposure risk for passengers traveling on long-distance high-speed trains, reported by Refs. [46–49]. The present work aims to investigate droplets transmission generated by coughing and surface contamination using the CFD model.

Transmission of the cough droplet in a high-speed train cabin were been previously investigated both in experimental and numerical approaches. For instance, Zhang and Li [50,51] applied CFD simulations to address the dispersion process of cough droplets of an individual in a high-speed rail cabin under different ventilation boundary conditions. As well, Wang et al. [46] numerically investigated the air distribution systems and the cough droplets dispersion in three different China railway high-speed train cabins to investigate the cough droplets removal ability. However, in both works, the authors stated that the effects of the location of the coughing passenger, particle size distribution, and modified air distribution system on droplets dispersion characteristics also needs to be further studied. In the current study, this gap has been covered by investigating the different strategies.

To achieve this, the fraction of particles suspended in the air inside the cabin, escaped of the exhausts, and most importantly the fraction of particles deposited on the face and body of passengers under different scenarios are separately examined, and then by comparing the results, which presented using the color contours, the passengers deal with the highest risk of infection, have been identified, which to our knowledge has, not been reported elsewhere. The investigation aims to understand the effects of temperature, relative humidity, ventilation rate, injection source, exhausts' location, and capacity, and the physical barriers on evaporation and transport of respiratory droplets to compare to alternative intervention measures that may be more economically viable such as using physical partitions between passengers on a full capacity cabin. The study considers a wide range of particle sizes (2 − 100 μm), which spans particles released during coughing [38,52]. We believe that our study and its findings are valuable to scientists and policymakers in our efforts to understand and reduce the transmission of SARS-CoV-2 in the global community.

2. Methods and materials

2.1. Train geometry

Fig. 1(a)-(d) illustrate the geometry of Long-distance High-Speed Train Cabin (LHSTC) selected for model analysis. The dimensions of the cabin are 13 m (L) × 2.8 m (W) × 2.4 m (H) with a volume of approximately 87 m³ (total fluid volume of approximately 65 m³), and the cabin includes 14 rows and 56 seats, according to seat-designs considered by Refs. [48,49]. The simulation domain of this study is one of the common LHSTC in the world. The geometry details were almost obtained from a real LHSTC geometry according to the [46–49]. The different parts of cabin and studied airflow input or exhaust positions are also marked. Fig. 1(a) and (b) show the passenger numbering and dimensions of different parts from each other on the top and front view of the domain. The sidewalls, east and west walls (Fig. 1(c) and (d)), is exposed to the outside of the cabin and has been mounted six large sealed windows on each of them. The north and south walls (Fig. 1(c) and (d)) toward the interior of the side cabins and each of them mounts a large door. The cabin's ventilation system is composed of 20 inlet vents (Fig. 1(c)). All inlet vents supply the same inflow rates and temperatures of air to create similar conditions. The type and size of inlets have been selected based on the model of the first type of Yang et al. study [47].

2.2. Mesh sensitivity

To make sure that the results are grid independent, a grid independence study was conducted, without droplets motion. The grid for the computational domain has been chosen after the following considerations. Four different types of grids, the number of elements are 1.8, 3.5, 4.2, and 5 ×10⁶ for the geometry, have been considered under the same boundary conditions (for details of boundary conditions see Table 1). ANSYS Fluent Meshing was used to generate the structured mesh for the computational domain. The outcomes of such a comparative study, are reported in terms of velocity magnitude and static temperature, have measured along a vertical line as located at $x_0 = x_1 = 6.5$, $y_0 = 0.5$, $y_1 = 2$, $z_0 = z_1 = 1.4$ (m), and is plotted in Fig. 2(a) and (b). All the results show a similar
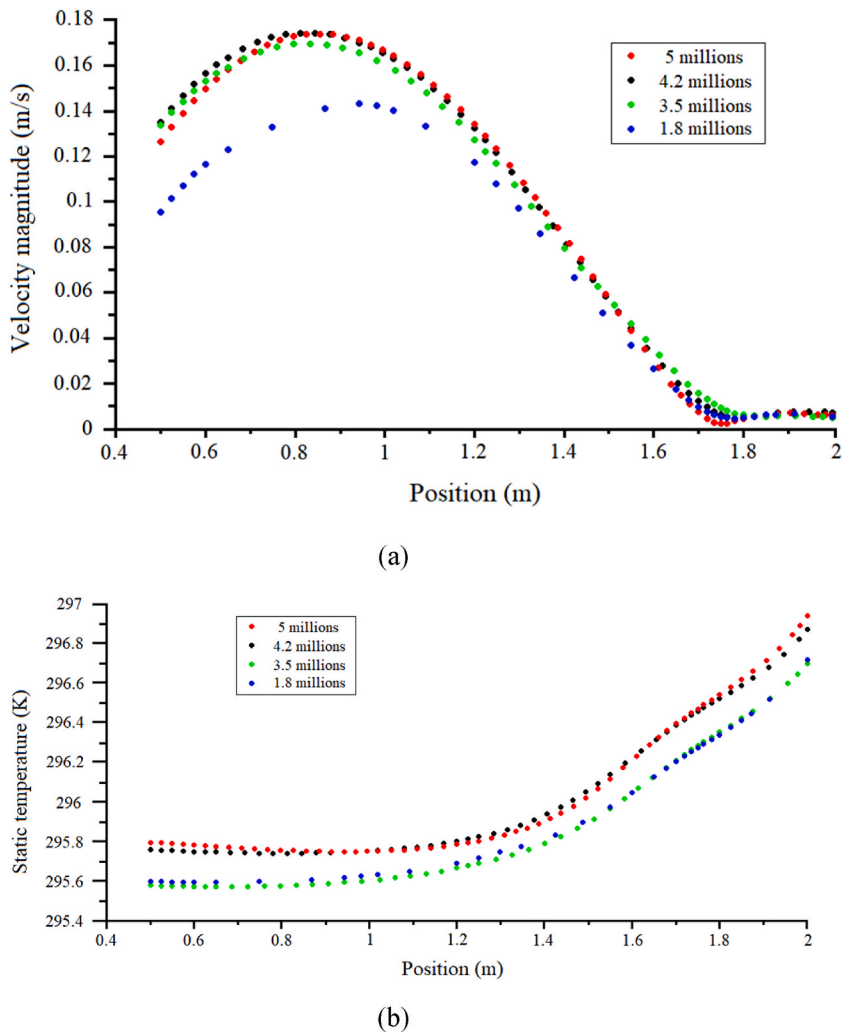
(a)

(b)

Fig. 2. Mesh sensitivity analysis. Comparison of the variation of (a) velocity magnitude, and (b) static temperature; over the selected line for studied mesh sizes.

variation. The difference between the mesh sizes of 4.2 and 5 million is very small. The significance of these figures resides in their ability to make it evident that all the examined grids can capture the counter-rotating vortices, especially in the upper part of the passenger cabin, in correspondence with the luggage compartment. It can be seen that the patterning behavior is essentially identical for the fine and finer grids, whereas a change in the symmetry of the main plume can be noticed when the coarse mesh is used. Based on these results and related arguments, a mesh with 4.2 million elements is used for the current simulation topic. In particular, the final mesh is reported in Fig. 3(a) and (b).

2.3. Computational fluid dynamics simulation

The airflow field in the cabin domain was solved using the incompressible Navier-Stokes equations. Six partial differential equations governing conservations of mass, momentum, turbulent kinetic energy (k), turbulent dissipation rate (ε), water vapor species transport, and temperature are discretized in spatial coordinates to acquire the steady-state solution. The SIMPLEC algorithm was employed for the velocity-pressure coupling. The steady-state solution is determined by an iterative process, starting from an initial guess for the steady solution in the physical domain. The initial guess in this study is set based on the hybrid initialization, which is performed by solving a Laplace's equation to determine the velocity and pressure field. The minimum remaining convergence scale was from the order of 10^{-4} in solving the flow field, and 10^{-5} for momentum equations and turbulence model. The continuous phase equations and discrete phase equations are solved alternatively. In other words, in the present study, first, the fluid field was resolved and then injected the particles were tracked using the Lagrangian framework by keeping the continuous flow solution constant. Standard $k - \varepsilon$ model obtained high reputation on predicting indoor airflows, although it might overestimate contaminants deposition [53].
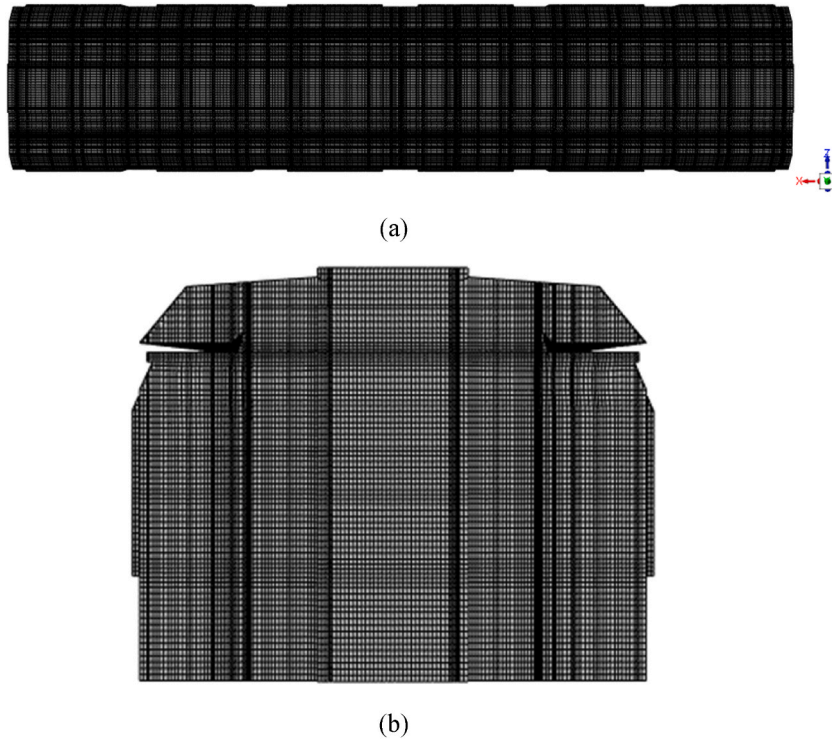
(a)

(b)

Fig. 3. Selected mesh for droplet evolution case is the fine one. (a) Top view, (b) front view.

2.3.1. Continuous (Eulerian) phase

The continuous carrier phase flow described by the RANS equations of for continuity, momentum, energy and species transport. The steady, incompressible and turbulent form of the equations are given below:

$$\frac{\partial \rho}{\partial t} + \nabla \cdot (\rho \vec{u}) = \dot{m} \tag{1}$$

$$\frac{\partial(\rho \vec{u})}{\partial t} + \nabla \cdot (\rho \vec{u}\vec{u}) = -\nabla P + \nabla \cdot \left[\underbrace{(\mu + \mu_t)(\nabla \vec{u} + \nabla \vec{u}^T)}_{\mu_{eff}} \right] - \nabla \cdot \left(-\frac{2}{3} \rho \kappa \vec{I} \right) + F_m \tag{2}$$

where $\dot{m}$ and F_m are the source terms account for mass transfer between the air and droplet due to evaporation. μ_{eff} is the effective viscosity considering both dynamic and turbulent viscosities.

In addition, species transport equations were solved to account for droplet evaporation (analytical equations of droplet evaporation process has been presented in supplementary data) and consequent changes in the droplet size. The mass fractions of water are solved by

$$\frac{\partial(\rho x_i)}{\partial t} + \nabla \cdot (\rho \vec{u} x_i) = \nabla \cdot \vec{J}_i + S_i \tag{3}$$

where S_i is the species source term and $\vec{J}_i$ is the diffusive flux of species i and can be expressed as

$$\vec{J}_i = -\left(\rho D_{i,m} + \frac{\mu_t}{Sc_t} \right) \nabla x_i - D_t \frac{\nabla T}{T} \tag{4}$$

where Sc_t is the turbulent Schmidt number and D_t is the turbulence diffusivity.

Heat transfer within the computational domain is accounted for by the following energy conservation equation:

$$\frac{\partial(\rho E)}{\partial t} + \nabla \cdot (\rho \vec{u} E) = \nabla \cdot \left(\left(\lambda_{eff} \nabla T \right) - \sum_i h_i \vec{J}_i \right) + S_h \tag{5}$$

where λ_{eff} is the effective thermal conductivity which considers both thermal conductivity of air, λ_a, and turbulent thermal conductivity, λ_t. And S_h is the thermal source term due to droplet motion and evaporation.

2.3.2. Adopted turbulence model

The standard k-ε turbulence model is used for the modeling of k, the turbulent kinetic energy (energy contained in velocity fluctuations), and ε, the dissipation rate of turbulent energy (rate of transfer of kinetic fluctuation energy to heat by viscous friction), as described in equations (6) and (7),

$$\frac{\partial(\rho k)}{\partial t} + \nabla \cdot (\rho \overrightarrow{u} k) = \nabla \cdot \left(\frac{\mu_t}{\sigma_k}\nabla k\right) + G_k - \rho\varepsilon \tag{6}$$

$$\frac{\partial(\rho\varepsilon)}{\partial t} + \nabla \cdot (\rho \overrightarrow{u} \varepsilon) = \nabla \cdot \left(\frac{\mu_t}{\sigma_\varepsilon}\nabla\varepsilon\right) + \frac{\varepsilon}{k}(C_{1\varepsilon}G_k - C_{2\varepsilon}\rho\varepsilon) \tag{7}$$

where $C_{1\varepsilon}$, and $C_{2\varepsilon}$ are constants 1.44 and 1.92, respectively, and σ_κ and σ_ε are 1.00 and 1.3, respectively. G_k is the production of turbulence kinetic energy.

Eddy viscosity μ_t is expressed as

$$\mu_t = \rho C_\mu \frac{k^2}{\varepsilon} \tag{8}$$

where C_μ is equal to 0.09.

2.3.3. Droplet tracking model

Discrete phase model (DPM) is employed to determine the transport of droplets generated by the respiratory events in ANSYS Fluent 2021 R2 software. Indeed, the DPM uses a hybrid Eulerian-Lagrangian framework, where the carrier phase is solved by Navier-Stokes equations, and the dispersed phase is solved by tracking a large number of droplet streams via the airflow field mean velocity. The droplets are transmitted via a phase consisting of a mixture of air and water vapor, and their pathways are affected by physical forces, turbulent dispersion, and the nature of the surrounding flow. The droplets' transport dynamics are tracked by equating the inertia force on droplets with external forces acting on the droplets (Newton's second law) [54]. The equation of motion of the spherical-shape droplets (subscript d) is given by:

$$\frac{Dx_d}{Dt} = u_d \quad , \quad m_d\frac{d\overrightarrow{u}_d}{dt} = \sum \overrightarrow{F} \tag{9}$$

where, m_d is the droplet mass and defined as follow

$$m_d = \frac{\pi}{6}\rho_d d_d^3 \tag{10}$$

In addition, here, F is the sum of all external forces exerted on the droplet. These external forces are presented in detail by the literature [54,55]. In the present work has been neglected pressure and virtual mass forces, as, the particles considered are small [54]. Furthermore, the effects of gravitation force, drag force, lift force, inertia force, and the effects of Brownian motion (for droplets less than 5 μm) on the coupling between the discrete and continuous phases are also included [56,57]. Due to the low volume fraction of the droplets/aerosols, we neglect droplet-droplet interactions. Thus, according to the above discussion, the equation of motion of a droplet (subscript d) is given by

$$m_d\frac{d\overrightarrow{u}_d}{dt} = \overrightarrow{F}_D + \overrightarrow{F}_G + \overrightarrow{F}_L + \overrightarrow{F}_B \tag{11}$$

where $\overrightarrow{u}_d$ and $\overrightarrow{u}$ are the droplet and air velocities, respectively. F_D is the drag force,

$$\overrightarrow{F}_D = \frac{18\mu_f}{\rho_d D_d^2 C_c}\left(\overrightarrow{u} - \overrightarrow{u}_d\right) \tag{12}$$

where D_d is the droplet diameter and C_c is the Cunningham correction factor and as given by

$$C_c = 1 + \frac{2\lambda}{D_d}\left(1.257 + 0.4e^{-(1.1D_d/2\lambda)}\right) \tag{13}$$

$$\overrightarrow{F}_G = (\rho_d - \rho)V\overrightarrow{g} \tag{14}$$

$$\overrightarrow{F}_L = 1.615\rho_d \nu^{0.5}D_d^2\left(\overrightarrow{u} - \overrightarrow{u}_d\right)\left|\frac{d\overrightarrow{u}}{dy}\right|sgn\left(\frac{d\overrightarrow{u}}{dy}\right) \tag{15}$$

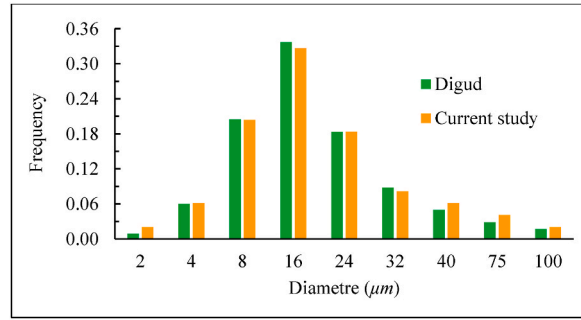$$\overrightarrow{F}_B = m_d G\sqrt{\frac{\pi S_0}{\Delta t}} \tag{16}$$

Fig. 4. Droplet size distribution of a single cough model.

$$S_0 = \frac{216 \, \nu k_{Boltzman} T}{\pi^2 \rho D_d^5 \left(\frac{\rho_d}{\rho}\right)^2 C_c} \quad , \quad k_{Boltzman} = 1.3806452 \times 10^{-23} \, J \Big/ K \tag{17}$$

G represents zero-mean, unit-variance, independent Gaussian random numbers, and T is the absolute temperature of the fluid (K).

The dispersion of droplets due to turbulence is modeled via a discrete random walk model (DRW). Indeed, in the DRW model, the effect of subgrid-scales flow on released aerosol/particle dynamics is considered by adding an eddy fluctuating velocity component to the average fluid velocity [58]. In other words, the instantaneous velocity is decomposed into the mean $(\overline{u}_f)$ and fluctuating (u_f') components as $u_f = \overline{u}_f + u_f'$ [59]. The average velocity of the fluid phase, is obtained by the RANS using the standard $k\text{-}\varepsilon$ turbulence model. Moreover, the fluctuating component (u_f') follows a Gaussian distribution based on the DRW model, which can be obtained following:

$$u_f' = \zeta \sqrt{\frac{2k}{3}} \tag{18}$$

where ζ is a normally distributed random number (accounts the randomness of turbulence).

Furthermore, the mass flow rate of droplets is calculated as:

$$\dot{m}_d = n\rho_d \frac{4\pi r_d^3}{3t} \tag{19}$$

where n is the total number of particles and t is the coughing duration time.

2.4. Boundary conditions

Fresh air is transported to passengers through the 20 supply air inlets located below the luggage carrier on each cabin side wall ($72 \, cm \, (L) \times 5 \, cm \, (W) \times 20 \, (number)$). The applied airflow velocities ranges have been selected in order to maintain the cabin air velocity under a comfortable level (i.e. less than $0.2 \, m/s$ [60]). Exhaust air exits have been installed in two different places, including the back of the seat on the floor and ceiling of the cabin. Fig. 1 shows the layout of seats and the corresponding air distribution system in the computational domain. The studied model contains 56 passengers, being seated in 14 rows. At the inlet of the air supply, a turbulence intensity of 5% and turbulence length scale of 0.035 m are assumed. The temperature of the lamps and LEDs is assumed to be 27 °C. For different ambient and airflow conditions, 17 cases were simulated and compared. In the CFD models, the sitting height of the passengers is $1.25 \, m$, and the total body surface area of each passenger is $1.47 \, m^2$. The passenger mouth area is assumed as $4 \, cm^2$ [37]. The face temperature of passengers is set at 36 °C. The boundary condition of the passenger is no slip. The simulated cough was assumed to have a fixed exhaled velocity profile, which conforms to typical values reported in the literature for velocity, duration, and total volume of air expelled. The duration of a single cough is $0.5 \, s$ and, the maximum coughing velocity is approximately $11.2 \, m/s$ [35,61]. The cougher coughs and expels a cone type jet with a typical flow rate at an angle of 30°. The droplets expelled by the cougher have a standard size distribution ranging from $2 \, \mu m$ to $100 \, \mu m$ (Fig. 4). The cough droplets are modeled to evaporate when droplet temperature is higher than the vaporization temperature. Since the exact composition of mucos-alivary fluid is unclear, salt is assumed to be the only non-volatile component in the droplet in this study. As per Duguid's study, droplets evaporate continuously to their dry nuclei state as they move in the air [38]. The size of the nuclei mentioned by Ref. [38] is around 20% of the original diameter. To achieve this, a volatile fraction of the water droplet is assigned as 98.2%, the remaining being a nonvolatile part. The number of expelled respiratory droplets assuming 4900 droplets per cough and a droplet size distribution measured by Ref. [38] shown in Fig. 4. A summary of boundary conditions used in the simulation have been presented in Table 1.

The droplet size distribution used in the study has diameters ranging from 2 to 100 μm [38], and as reported in the literatures [39, 41], evaporation time for 10 μm droplets is greater than 0.05 s, the time steps are selected such that evaporation is captured accurately. Due to the evaporation, the droplet diameter reduces to a dry nuclei state, and after that, no evaporation of droplet occurs [41]. The time step size of 0.005 s during evaporation was completed (to 10th second) and 0.05 s after the evaporation is employed for the
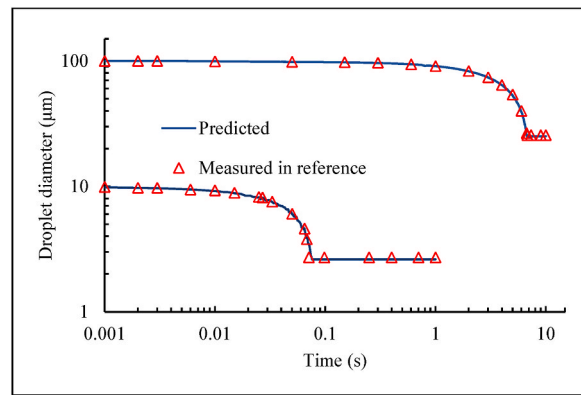
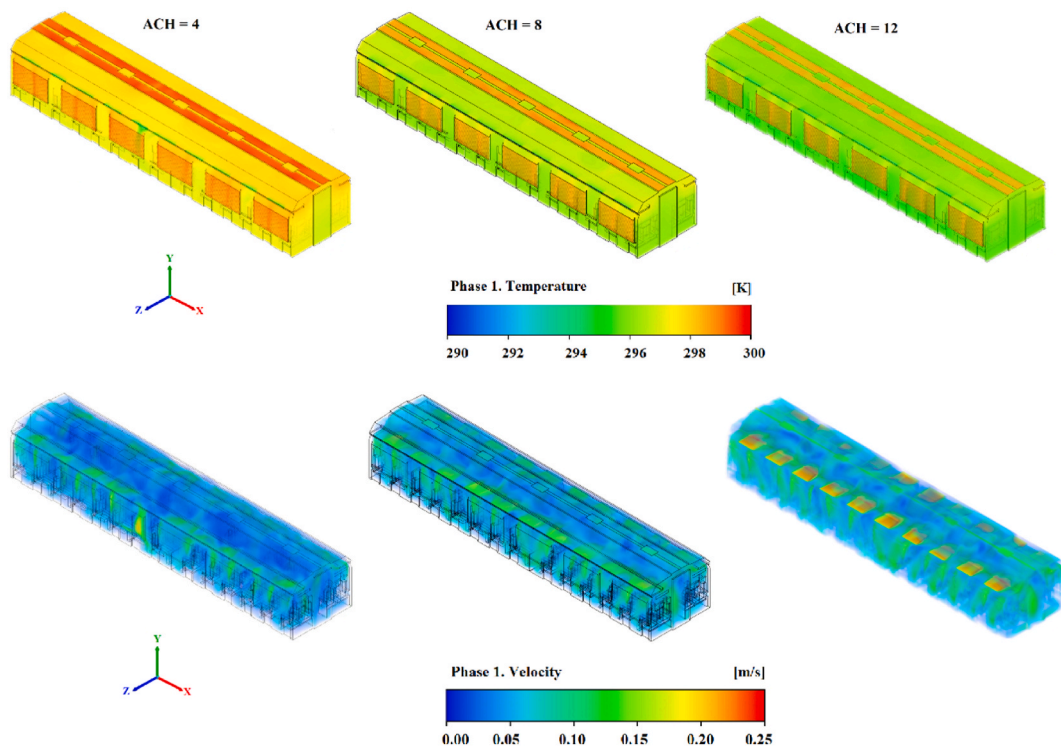**Fig. 5.** Model validation using data from Li et al. (2018).

Fig. 6. Isometric view of the volume rendering of airflow temperature (first row) and velocity (second row) inside the cabin for the three different ventilation rates, including 4, 8, and 12 ACH.

simulations, ensuring the stability criteria.

2.5. Validation

The evaporation modeling of droplets in this work was compared with Li et al. study [62]. Furthermore, the accuracy of the model was checked with results research by Shao et al. [63] and Ahmadzadeh et al. [13] works, after a good acknowledgment and agreement, we implemented the solution results. For instance, in the following section, we have presented the comparison verification results from Li et al.

The calculation domain of Li et al. work is an enclosed room (4 m × 3 m × 2 m) at a constant temperature of 25 °C. Two different size droplets of initial diameters of 10 and 100 μm are evaporated under dry conditions. In this model, it was assumed that single droplets were released one after another with a time-frequency of 0.01 s at 37 °C. Droplets consist of two parts: 1) 98.2% water, and 2) 1.8% nonvolatile particles, with a density of 1000 kg/m^3. The multicomponent Eulerian-Lagrangian approach is employed to realize mechanistic modeling. For the simulation, the structured hexahedral method was used, which consists of over 600,000 elements. The predicted time-dependent diameter (solid lines) of droplets injected by coughing was compared against the theoretical results
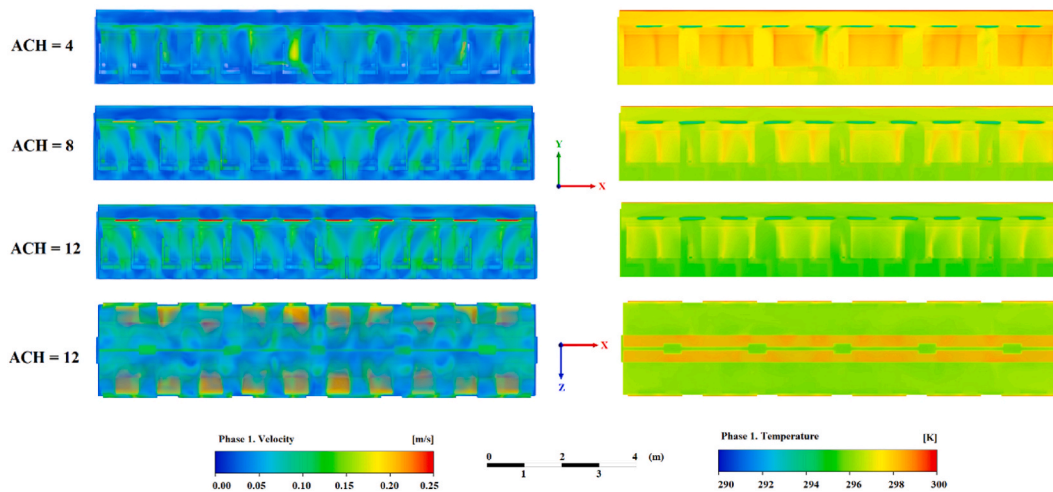
Fig. 7. Volume rendering of the velocity and temperature fields on XY plane for the three different ventilation rates, including 4, 8, and 12 ACH, and on XZ plane (last row) for 12 ACH case.
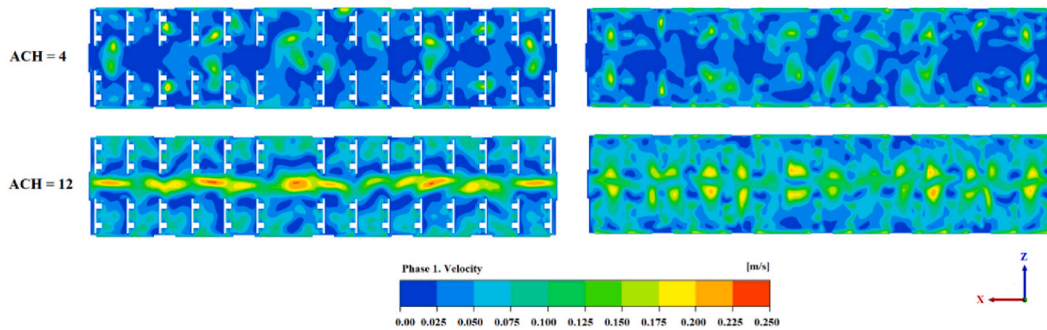

Fig. 8. Airflow velocity contours at two distinct heights on horizontal planes: y = 1 m (left side), and y = 1.5 m (right side) for 4 and 12 ACH ventilation rates.

(triangular markers). As shown in Fig. 5, a satisfactory agreement can be observed between the numerical results of this study and the data reported in the literature. Moreover, more details of the droplet evaporation model and equations have been provided in Appendix A-supplementary material.

3. Results

3.1. Results of continuous phase

This section mainly presents the results of numerical simulations is related to evaluating the impact of the various ventilation rates (4, 8, and 12 ACH) on airflow field distribution. The airflow distribution performance of these ventilation rates is compared and selected the best case in terms of the thermal comfort considerations. Then, with reference to specified and effective ventilation rate, droplet dispersion is calculated and discussed in line with infection risk assessment indicator, aiming to provide guidance on the design and implementation of suitable airflow conditions and physical barriers as an efficient disease transmission mitigation strategy. Fig. 6 shows a volume rendering of airflow temperature and velocity in the whole cabin areas for the three different ventilation rate, including 4, 8, and 12 ACH. In each case the initial and boundary conditions, except the inlet velocity, are the same. The results show that by increasing the ventilation rate, the temperature inside the cabin decreases more rapidly and approaches the comfort conditions in the warm season. This is because, in case 12 ACH, more areas of the cabin are affected by the cold supply airflow (according to second-row results), resulting in more energy exchange with the surrounding molecules than in cases 4 and 8 ACH. The other worth point is to observe high-temperature areas near windows and lighting systems. In this study, fixed temperature boundary conditions for lighting systems (of 30 °C) and windows (of 28 °C) have been employed to approach the real situation. That is why in the presented results we see high temperatures in these areas. The temperature of these areas also shows a further decrease by increasing the supply velocity by following the temperature of the whole cabin area.

As well, the simulated volume rendering of the velocity and temperature fields on the longitudinal planes (XY and XZ planes) are shown in Fig. 7 for the three simulated cases. The air temperature in similar points in case 1 is approximately 2 °C higher than case 3, on the other words in case 1 passengers experienced the warmer conditions than case 3. The air temperature close to the passengers is
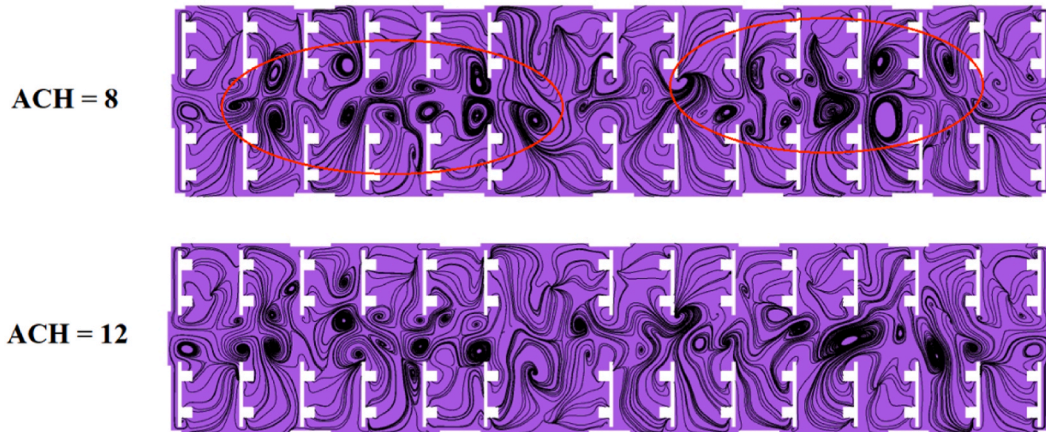
Fig. 9. Streamlines and recirculation zone during cases 2, and 3 at horizontal ($y = 1\,m$) plane.

Table 2
Study scenarios to determine the effects of ventilation rates.

Scenarios	The desired effects						
	Ventilation rate (ACH)	RH (%)	Emission source	Exhaust's location	Temperature (K)		Physical barrier
					T_{in}	T_{out}	
1	4	50	C7	Mode 3[a]	293	300	No
2	8						
3	12						

[a] For details refer to Fig. 14.

slightly higher because of the heat flux released from the human body (thermal plume). What is more evident in these figures is the variations and fluctuations of the temperature and velocity field around the passengers. The cause of these fluctuations is due to the thermal plume generated by the heated manikin (32.2 °C) pulled the flow toward its body, dramatically altering its trajectory in the cabin. As illustrated, it can be concluded the thermal plume plays an important role in the distribution of the both flow fields and droplets in indoor environments [64,65]. This mechanism is such that since the body temperature of passengers is higher than their surroundings, and according to this principle of convective energy transfer: energy is transferred from the hot zone to the cold zone, so the molecules around the passengers have more motions, and result in appreciable velocity and temperature fluctuations in these areas than other cabin domain.

Fig. 8 shows the airflow velocity contours at two distinct heights (horizontal planes): $y = 1$, and $y = 1.5\,m$. The airflow velocity distribution is approximately homogeneous in the longitudinal direction, especially in case 3. For a cabin mean temperature requirement in summer of $23 - 25\,°C$, the maximum airspeed allowed is $0.4\,m/s$. As the reader will realize by inspecting this figure, on both horizontal planes in case 1, the mean velocity field is under the target value.

To find out the influences of the formation of flow vortices and recirculation zones on the particles' shelf life inside the domain, Fig. 9 provides a comparison between streamlines and recirculation zone in cases 2, and 3 at horizontal ($y = 1\,m$) plane. In both scenarios, the formation of recirculation zones between rows, with different strengths and areas, is observed. But what important point that cause the difference between these comparisons is that by increasing the ventilation rate the vorticities area is reduced and moved in the middle of the cabin. Especially when the airflow velocity is low, the flow momentum is weak to overcome obstacles such as the bodies and seats, and this leads strong and large recirculation areas between the rows relative to the high airflow velocity. These differences indicated by red lines in Fig. 9.

3.2. Results of dispersed phase

In this section, initially the studied scenarios in each case defines and then presents the results.

3.2.1. Effects of ventilation rate

In this section, the effects of ventilation rate on droplet transmission and shelf-time inside the domain are investigated. To display these impacts, three different ventilation rates, including 4, 8, and 12 ACH, have been selected based on the thermal comfort requirements of public transport systems (study scenarios presented in Table 2). Here, the relative humidity and the temperature are kept fixed at 50% and 303 K respectively.

The effect of ventilation rate on suspended (in-fluid) and escaped particles over time is shown in Fig. 10(a) and (b), respectively. As expected and shown, increasing the airflow ventilation rate improves particle exit conditions and decreases their residence time. In
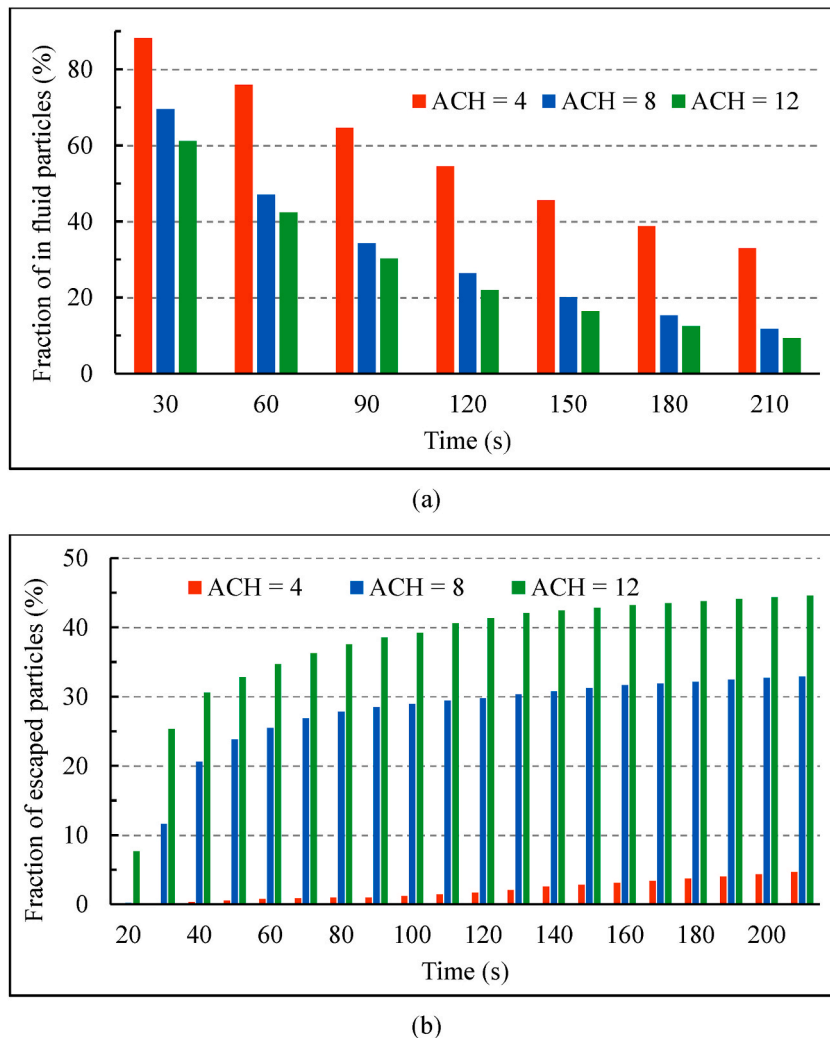
(a)

(b)

Fig. 10. Analyze the effect of ventilation rate on the fraction of: (a) suspended, and (b) escaped, particles over time.

addition, when the airflow velocity triples, over time from 60 s onwards, the fraction of the suspended particles is reduced by more than one-third. Another noteworthy point relates to the difference in the suspended fraction particles variations during these three ventilation rates. This difference is greatly reduced by increasing the ventilation rate. For example, after 210 s, the difference decreased from 21% to 2.5%. This indicates that the ventilation rate of 4 ACH has a poor performance in reducing environmental pathogens compared to rates 8 and 12 ACH. Therefore, it can be concluded that ventilation rates of 8 and 12 ACH have approximately the same performance as the indoor air purification, although rate 12 ACH shows the best performance in reducing particulate matter compared to the other two values at the same time and conditions. This poor performance can also be seen by comparing the variations of the fraction of escaped particles from the environment over time under the various ventilation rates (Fig. 10(b)). It is due to that by increasing the ventilation rate, the momentum of airflow raise and result in they overcoming the physical forces exerted by the particles, this leads to a large portion of the particles being carried with the airflow, enforce them to follow the flow streamlines created towards the exhausts. The quantities analysis of particles released from the environment at the end of the 210th second also indicates doubling and tripling the ventilation rate accelerates the volume of the exhaust particles by more than 7 and 10 times, respectively this issue.

3.2.2. Effects of relative humidity

Fig. 11(a) and (b), shows the effects of RH on the fraction of suspended and escaped particles, respectively. The ambient temperature is fixed at 303 K and the relative humidity is varied as 25%, 50% and 75% (study scenarios presented in Table 3). The results emphasize the RH has a significance role on particle shelf-time and resulting on infection risk. At low RH, the evaporation rate of the droplets is high and results in the decline of the mass of droplets is fast, thus, we see a long shelf life of the droplets in the environment. Increasing the relative humidity of the supply airflow accelerates the process of particles leaving the environment and reduces the fraction of suspended particles. This, in turn, will reduce the risk of infection.
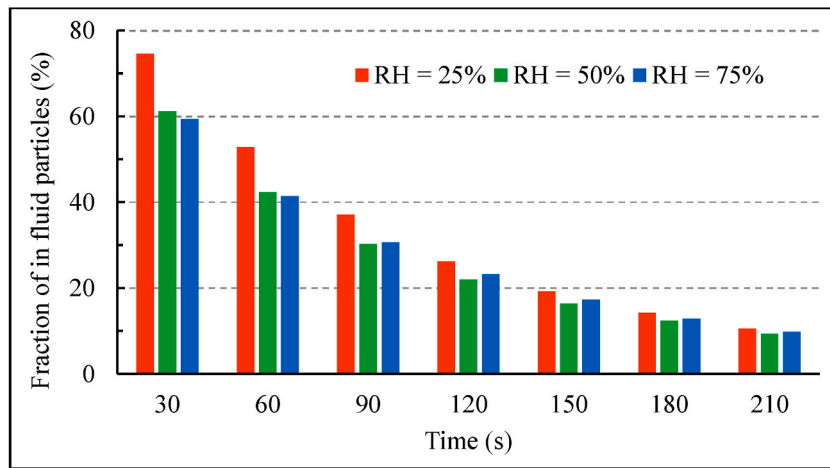
(a)
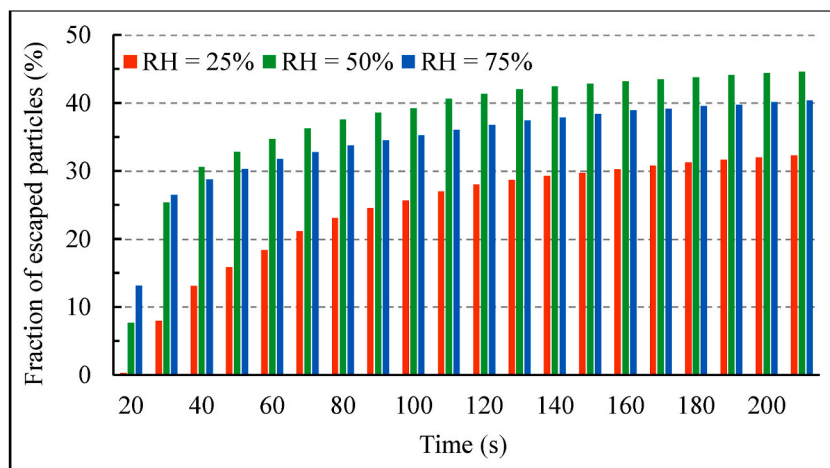
(b)

Fig. 11. Analyze the effects of RH on the fraction of: (a) suspended, and (b) escaped, particles over time.

Table 3
Study scenarios to determine the effects of RH.

Scenarios	The desired effects						
	RH (%)	Ventilation rate (ACH)	Emission source	Exhaust's location	Temperature (K)		Physical barrier
					T_{in}	T_{out}	
1	25	12	C7	Mode 3	293	300	No
2	50						
3	75						

The magnitude of the droplet mass variations over time in terms of three various parameters, which include droplets' initial (solid lines), final (dot lines), and changed (dash-dot lines) mass, have been compared for three RH in Fig. 12. To interpret the results of this figure, we first define these parameters. The final mass of the droplets is the result of subtracting the initial mass from the changed mass at the same time. On the other hand, the mass change of droplets arises from two factors, which are: 1) the exchange of mass and energy with the surrounding flow and, 2) the reduction of mass by settling on surfaces or/and leaving the environment. The first factor is important as long as the droplets still have water content. As soon as the water content of the droplet is completely evaporated, then this factor loses its role and the reduction in particle mass will be related only to the second factor. Therefore, considering the size of the particles distributed in this study, it can be said that the first factor in the first 8–9 s will play a colorful role in reducing the mass of the droplets. Which is visible in the enlarged part of the figure. This parameter has a negative sign because it shows the decrease in droplet mass over time, but for better reasoning, its magnitude results are shown in this figure. The initial mass refers to the mass of the
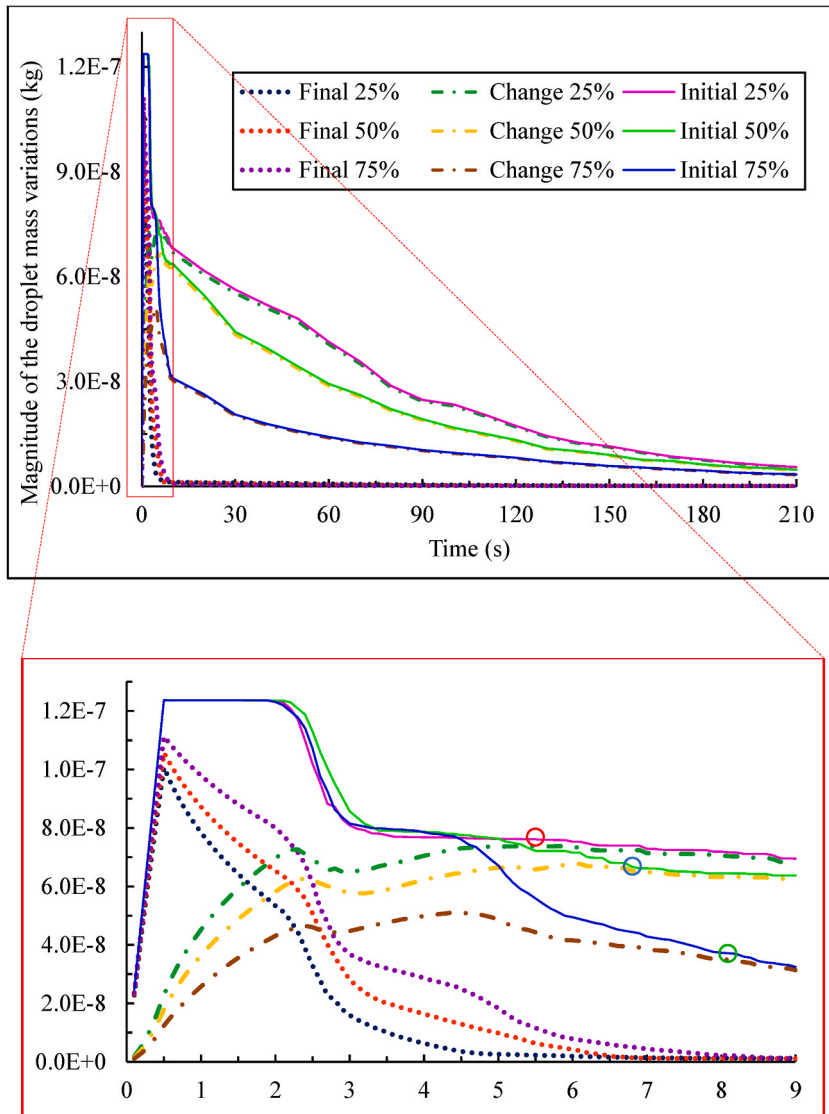
Fig. 12. The magnitude of the initial, changed, and final droplet mass variations over time, and the effect of RH on droplet evaporation at the fixed ambient temperature.

droplets in the domain at a given moment without considering these two factors. As shown, these parameters decrease over time for all three RH cases. Because the mass of the droplets decreases over time due to droplets' evaporation, deposition on the surfaces, and exit the domain. But what is important and expected is that the changes are different for the RH studied. This is due to the nature of the mass and energy transfer between the droplets and the surrounding airflow at different relative humidity. As shown in Fig. 12, as the relative humidity of the cabin airflow increases, the slope of the mass changes becomes steeper. In other words, the droplet mass reduction at high relative humidity is higher than low relative humidity. Another noteworthy point is the changes in the final mass of the droplets, the slope of their decreasing trend of which remains almost constant from 10th seconds onwards. Because most of the droplet volume (98.2%) is composed of water as a result, by evaporates the water content, which usually takes less than 10 s, the mass of the droplets decreases increasingly, and after this moment, the reduction of the particle mass is only due to deposition on the surfaces or leaving the environment. Moreover, with the increase in evaporation time, the final size of the droplet increases. This can be attributed to the fact that when the relative humidity increases, the final water content at a higher relative humidity is more. To examine more accurately the nature of the droplet mass reduction phenomenon due to the evaporation process of droplets' water content, the variations trends have been magnified in the first 9 s. An important point that can be mentioned according to the following results is that increasing the relative humidity increases the time required for the water content of the droplets to evaporate. This conclusion derives from the point that the variations of the initial and final droplets' mass begin to tangent together at that point. These points have been marked as hollow circles of red, blue, and green, which correspond to the relative humidity of 25, 50, and 75%, respectively. As can be seen, the green circle occurred later than the previous two circles. This means that the time required for the
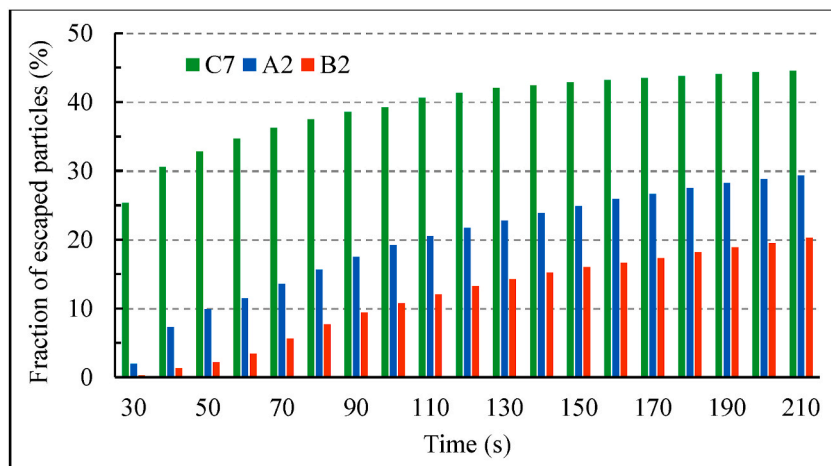
Table 4

Study scenarios to determine the effects of emission source.

Scenarios	The desired effects						
	Emission source	Ventilation rate (ACH)	RH (%)	Exhaust's location	Temperature (K)		Physical barrier
					T_{in}	T_{out}	
1	A2	12	50	Mode 3	293	300	No
2	B2						
3	C7						
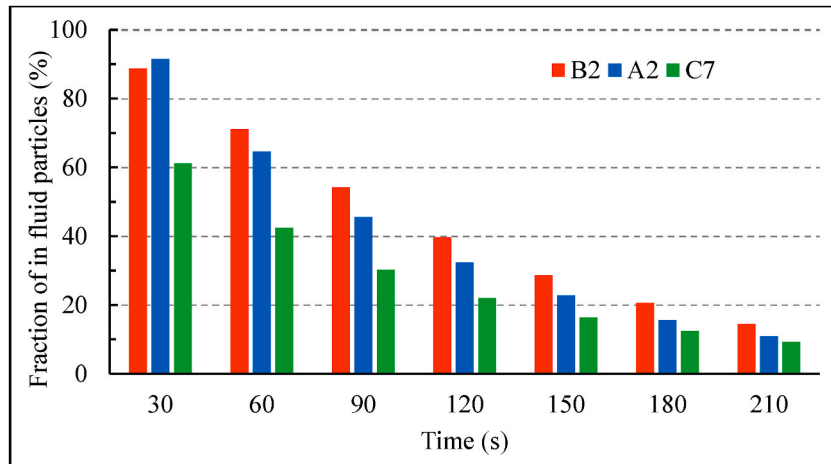
(a)

(b)

Fig. 13. Analyze the effects of emission source on the fraction of: (a) suspended, and (b) escaped, particles over time.

droplets to evaporate increases with increasing humidity. Another important result relates to the variations of the final mass of the droplets. As can be seen, at the end of the droplet injection, 0.5th second, despite the evaporation process, the variations are increasing over time. However, immediately after the particle injection is completed, the variations approach changes direction at once and take a decreasing trend. This decreasing process continues with a steep slope until all the water content of the droplets has completely evaporated. Then the final mass of the particles decreases with a very low slope. In addition, it is observed that at high relative humidity, the particles' evaporation ends late (from a comparison of dotted graphs).

3.2.3. Effects of emission source

To evaluate the effect of patient passenger location on the particle dispersion, the following comparison was performed for three different emission sources, including passengers A2, B2 and C7 under the same conditions. Here, the relative humidity and the
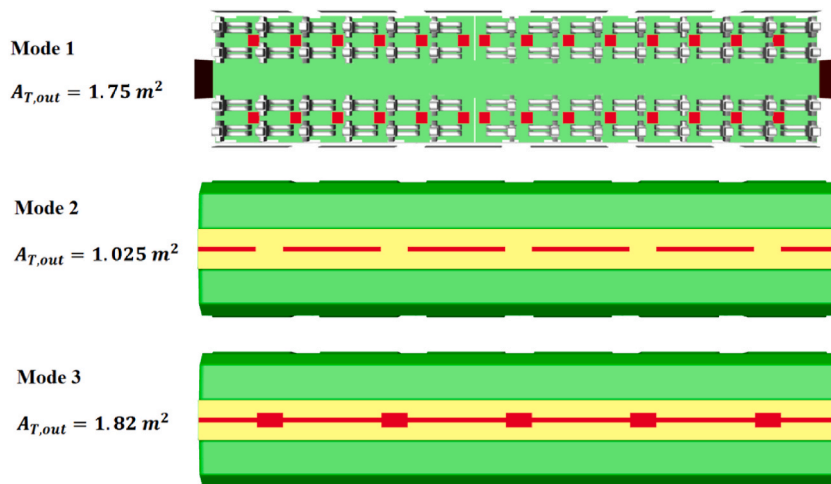
Fig. 14. Introducing the three different modes of exhausts location.

Table 5
Study scenarios to determine the effects of exhaust's location and capacity.

Scenarios	The desired effects						
	Exhaust's location	Ventilation rate (ACH)	RH (%)	Emission source	Temperature (K)		Physical barrier
					T_{in}	T_{out}	
1	Mode 1	12	50	C7	293	300	No
2	Mode 2						
3	Mode 3						

temperature are kept fixed (study scenarios presented in Table 4).

Fig. 13(a) and (b) show the effects of emission source on the fraction of suspended and escaped droplets over time, respectively. The results indicate that patient location plays a significant role in the infection risk of healthy individuals. According to the results, when the C7 passenger is assumed to be patient, the in-fluid particle variations over time faster than the other two, also, particles can leave the environment at high rates. Its reason refers to the nature of the formation of the vorticity and circulation zones. As shown in Fig. 13 (a), the C7 location is farther from the front passenger than the A2 and B2 occupants, so that airflow does not collide with physical objects such as the seats, and this causes vorticity and circulation zones formed in the area are weaker and smaller than locations A2 and B2 (see Fig. 9). Because the particles trapped in these areas travel in a vorticities, this allows such particles to have a long shelf life in the environment. These observations can also be expressed for comparison between two A2 and B2 passengers. However, in this case, in addition to the basic role of circulation flows, the role of the luggage can also play an important role in creating different results.

3.2.4. Effects of exhaust's location and capacity

Other parameters that play an important role in the dispersion of particles and thus in the intersection of the risk of infection in indoor environments are the location and capacity of the exhaust. In this section, to clarify these effects, the results for three different modes, as shown in Fig. 14, are presented and discussed. Here, the relative humidity and the temperature are kept fixed (study scenarios presented in Table 5).

As illustrated in Fig. 15(a) and (b), changing the exhaust location (between modes 1 and 2) and increasing the exhaust capacity make considerable differences in the fraction of the suspended and escaped particles. But the effect of these factors on the exit of particles from the domain is more noticeable. Comparison of the results of Fig. 15(a) and (b) indicates that the displacement of the exhausts from the floor to the ceiling of the cabin has a significant effect on both the shelf life of particles and the exit of particles in relation to the increase of the exhaust capacity. Because most of the injected droplets evaporate in the first moments, this reduction in mass causes the aerodynamic forces to overcome the force of gravity and move the particles upwards. This is a potential factor that causes to escape of more particles from the ceiling exhausts than from the floor ones.

3.2.5. Effect of physical barrier

One of the non-invasive and low-cost ways to reduce the risk of pathogens in indoor environments is to use the physical barriers. The effectiveness of this strategy in reducing the risk of infection and transmission of infectious particles has been examined and proven. The results of these investigations also have been presented similar to the previous sections in the framework of the variation rate of the fraction of suspended and escaped particles versus time are shown in Fig. 16(a) and (b). Here, the relative humidity and the
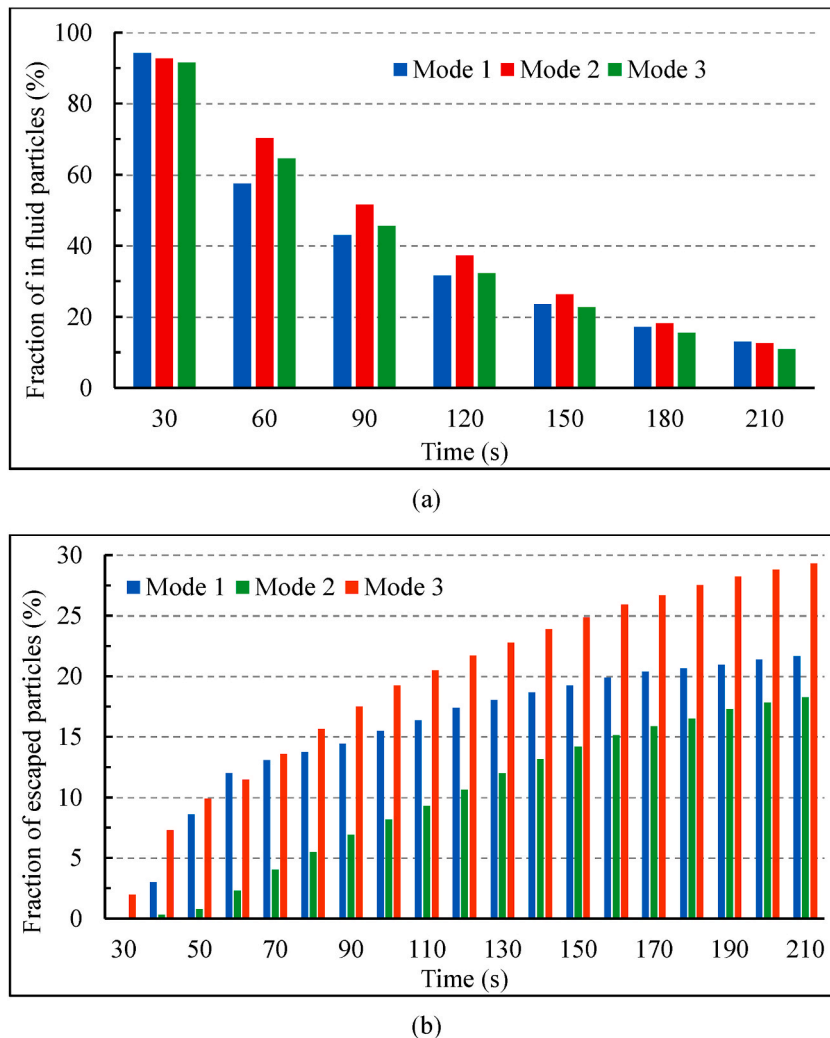
(a)

(b)

Fig. 15. Analyze the effects of exhaust's location and capacity on the fraction of: (a) suspended, and (b) escaped, particles over time.

temperature are kept fixed (study scenarios presented in Table 6). And the ventilation rate is 12 ACH.

The results show that the presence of physical barriers strongly affects the shelf life of particles. In such a way that after about 1 min of simulation time, the fraction of suspended particles in presence of physical barriers implies a reduction of more than 50% compared to the case where there are no barriers. For example, at the end of the 160th second, the fraction of suspended particles in the presence of barriers of 6.2%, while the same quantity in the absence of barriers is equal to 14.8%, i.e., an 8.4% reduction in particles number. A similar performance of the presence of physical barriers can be attributed to the acceleration of particle exit. Another noteworthy point is that the variation slope of the exited particles from 60th seconds onwards remains almost constant. This is due to the high reduction of airborne particles in this scenario. On the other hand, after 1 min, the final state of 78% of the particles is determined, i.e., they have been deposited or escaped. The location and dimensions of the physical barriers are illustrated in Fig. C1 and C2 (Appendix C).

3.2.6. Effects of the temperature

Temperature is one of the main elements of droplet evaporation. In this section, the effects of three different input flow temperatures on the shelf life and the spreading of particles have been measured. Temperatures have been selected so that there is a 7-degree temperature difference between the input and exhaust flows in all three scenarios.

The results of Fig. 17(a) and (b) show that increasing the temperature increases the shelf life of the particles in the environment. And this is almost obvious because increasing the temperature accelerates the process of particle evaporation and leads to a higher reduction of the droplet mass than the low temperatures. This implies that the particles become light and able to travels further distances. As a result, the descending slope of the variation rate of the suspended particles at high temperatures is lower than the low temperatures. Moreover, low temperatures have a good performance in relation to escaping the particles. Fig. 18 shows the effect of temperature on droplet evaporation. Here, the relative humidity is kept fixed at 50% and the supply temperatures are 290 K, 293 K, and 298 K (study scenarios presented in Table 7). The first thing which can be observed is that the residual droplet size (final mass of
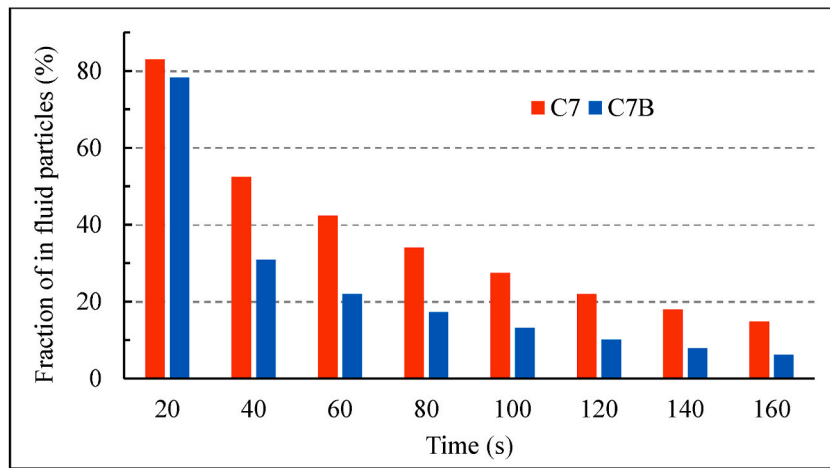
(a)
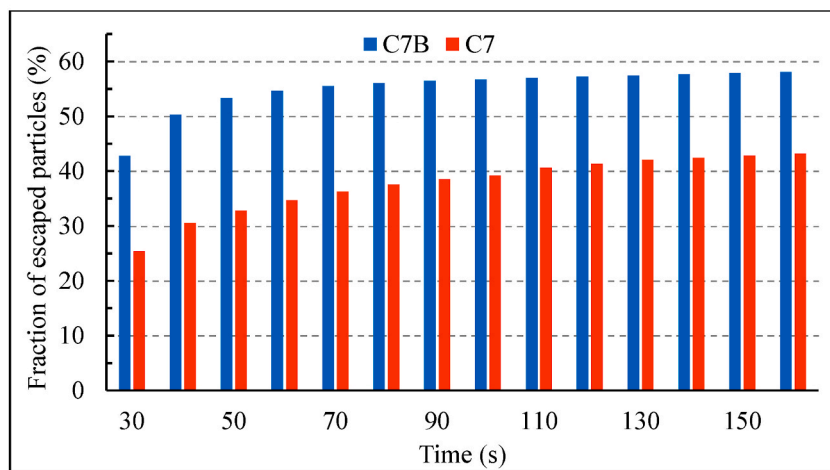
(b)

Fig. 16. Analyze the effects of physical barrier on the fraction of: (a) suspended, and (b) escaped, particles over time.

Table 6
Study scenarios to determine the effects of Physical barrier.

Scenarios	The desired effects						
	Physical barrier	Ventilation rate (ACH)	RH (%)	Emission source	Temperature (K)		Exhaust's location
					T_{in}	T_{out}	
1	No	12	50	C7	293	300	Mode 3
2	Yes						

droplets) at all the temperatures is equal at the end of the evaporation and this is because the residual water content amount in the droplet is dependent on the relative humidity and relative humidity being constant, as a resulting the water amount remains the same. Although, an increase in the supply temperature accelerates the evaporation process because at such conditions the surrounding environment will supply latent heat to the droplet to help evaporation, and also, the surrounding environment with higher temperature has more water holding capacity than the surrounding environment with low temperature. Nonetheless, at lower temperatures like 290 *K*, the droplet evaporates by utilizing its own surface heat and there is no further supply of latent heat from the surrounding environment as the ambient temperature is lower than the initial droplet surface temperature. And these are the reasons, that lead to more droplets deposited on the surfaces at lower temperatures than higher temperatures and we observed the final mass of droplets variations slope at a lower temperature is sharper than warmer conditions.

Besides, by comparing the magnitude of the variation rates of the droplets' changed mass when the target is the cooling of the environment, i.e., the input temperatures of 290 and 293 K, we conclude that in the first 8 s, as the temperature increases, the reducing
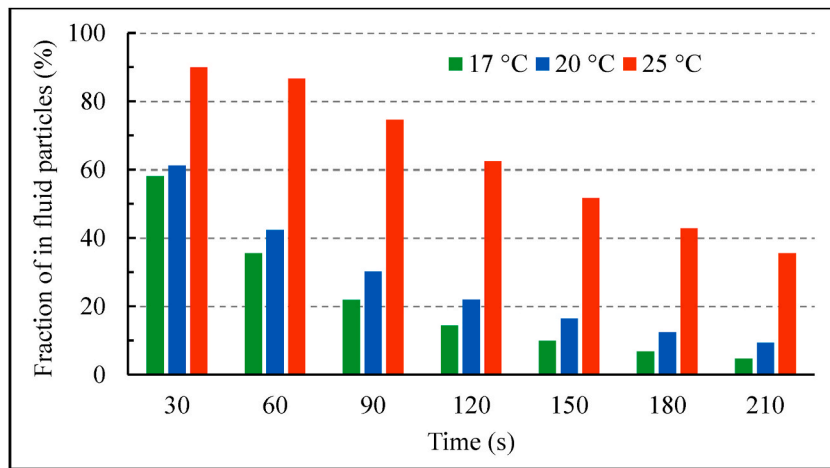
(a)
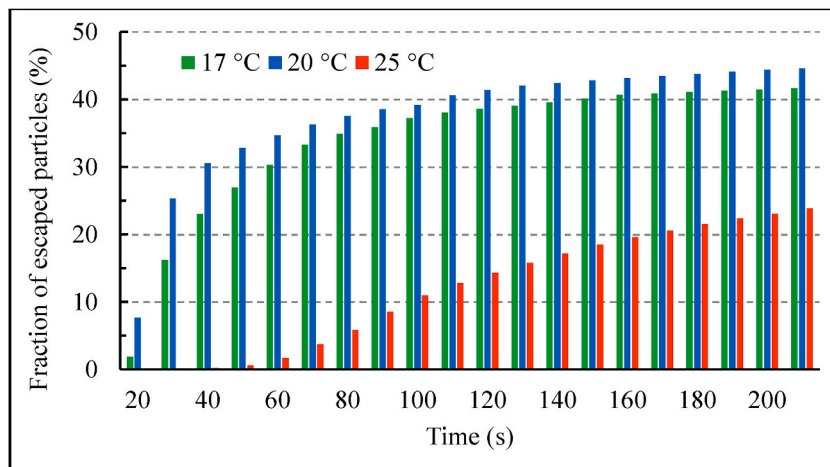
(b)

Fig. 17. Analyze the effects of the temperature on the fraction of: (a) suspended, and (b) escaped, particles over time.

mass of the droplets hasten.

Therefore the RH and temperature effects' results revealed that higher RH and low temperature slows down the evaporation rate and restricts the amount of water leaving the droplet surface, which, in turn, increases the evaporating duration. Fastest evaporation for the droplets can be seen at 293 K and 25% RH and the slowest evaporation is at 290 K and 75% RH. Thus, it can be concluded that the high temperature-low humidity is an ideal condition for droplet evaporation because the high-temperature environment will be a source of latent heat, and low RH will allude to more water holding capacity and thus favor the evaporation. Comparing the different droplet sizes show that small droplets evaporate faster than large droplets in whatever the ambient condition. In other words, larger droplets experience a delay in the evaporation time scale due to their larger volume to surface area ratio.

4. Discussion

After discussing the results of different effects on the spread and shelf life of droplets from a patient's cough in the previous section, in the present section to better understand the performance of each of the presented scenarios, we discuss their results in the form of comparative contours. The results of the individuals' infection risk have been presented separately for different scenarios by evaluating the fraction of particles deposited on the body (figures a) and on the face (figures b) of healthy passengers. These contours can be very useful in applying and making better and more accurate decisions for preventive measures. In all scenarios, the patient has been marked in yellow.

4.1. Ventilation rate assessment

Fig. 19 shows the zones and number of healthy passengers exposed to a high risk of infection in terms of the suspended particles and trapped particles on the face and body of them. As the ventilation rate increases, both the particle residence time and the number of
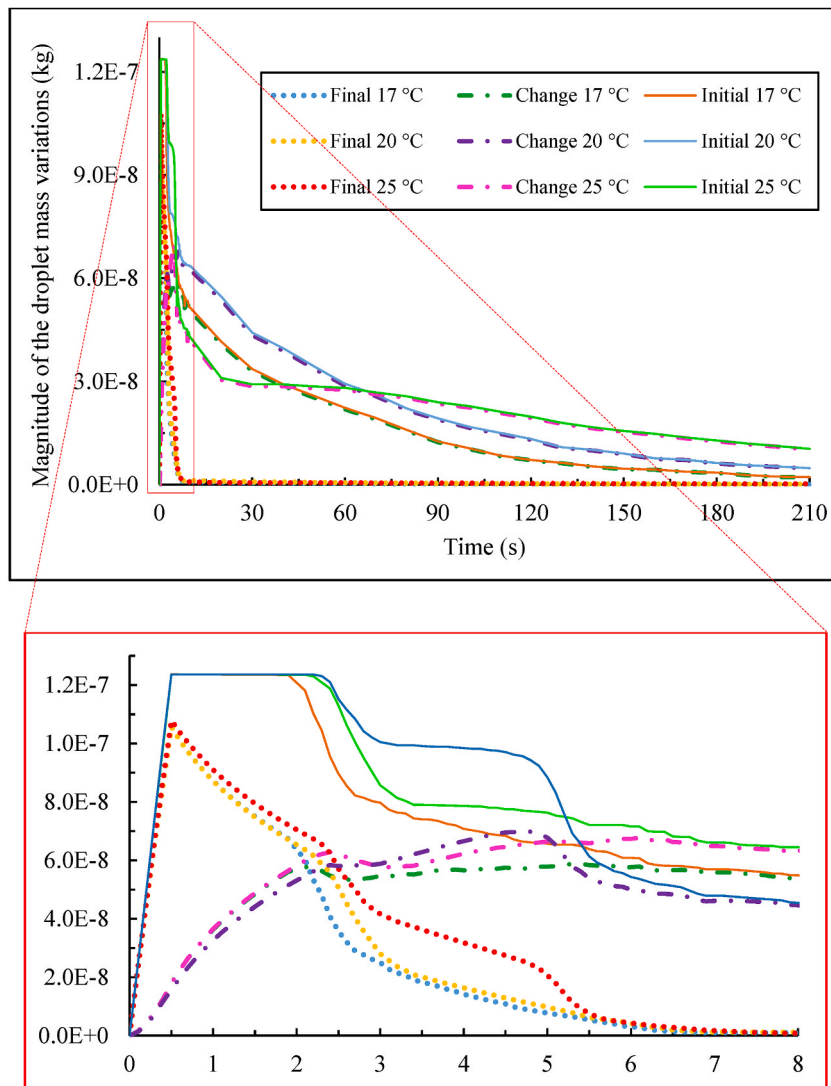
Fig. 18. The magnitude of the initial, changed, and final droplet mass variations over time, and the effect of temperature on droplet evaporation at the fixed RH.

Table 7
Study scenarios to determine the effects of the supply temperature.

Scenarios	The desired effects		Ventilation rate (ACH)	RH (%)	Emission source	Exhaust's location	Physical barrier
	Temperature (K)						
	T_{in}	T_{out}					
1	290	297[a]	12	50	C7	Mode 3	No
2	293	300[a]					
3	298	291[b]					

[a] Purpose is cooling.
[b] Purpose is heating.

people at risk decrease. From the results of Fig. 19(a), it can be concluded that passengers sitting in the front, rear and side rows of the infected passenger are at the highest risk of infection compared to other passengers. As the ventilation rate increases, the risk intensity in these people also decreases. This performance can also be found in Fig. 19(b).

4.2. RH assessment

A comparison between the relative humidity studied in this work implies that at 75% relative humidity, due to the delay of the
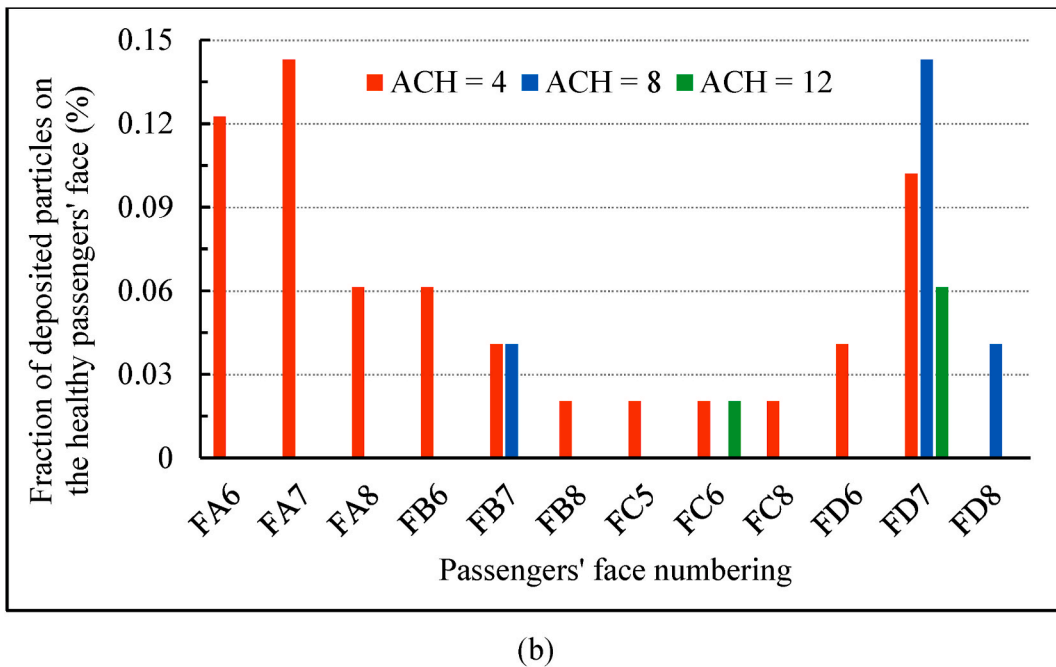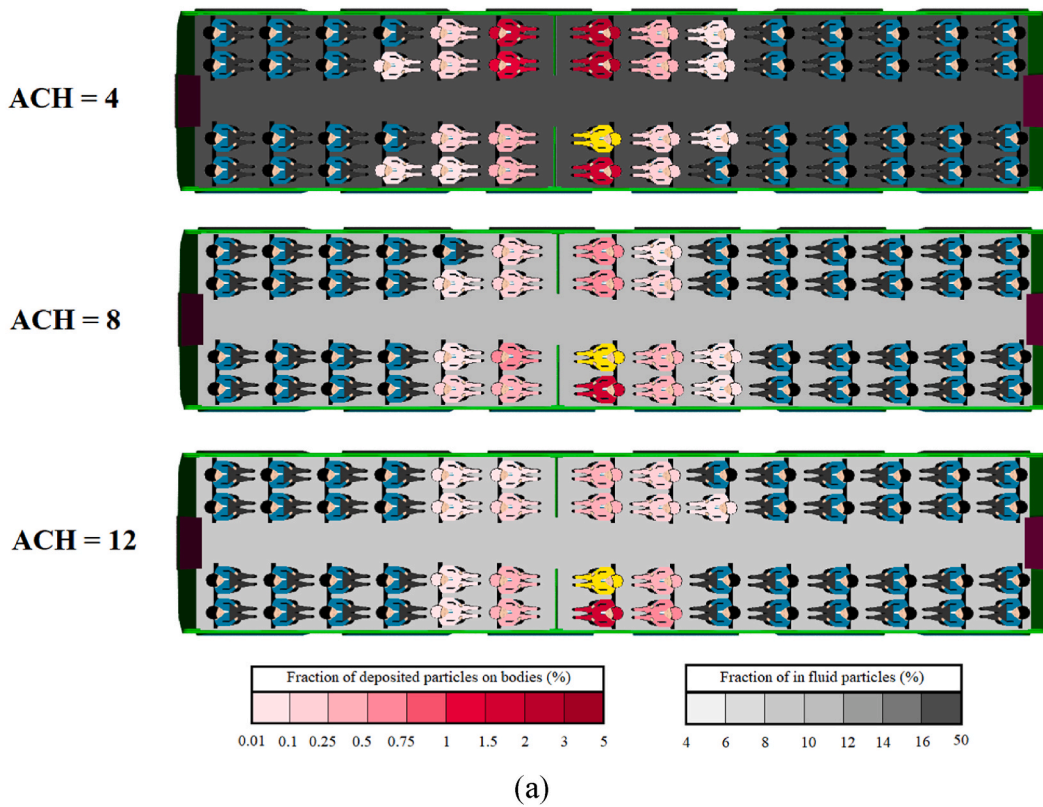
(a)

(b)

Fig. 19. Infection risk analysis for different ventilation rates. (a) Contours of fraction deposited particles on healthy passengers' body and suspending particles in air, and (b) fraction of deposited particles on the healthy passengers' face.

evaporation process, the penetration length of the particles inside the cabin increases. Furthermore, the results of Fig. 20(a) and (b) indicate that the selection of the medium relative humidity of 50% can be a more favorable role against the infection of healthy passengers.
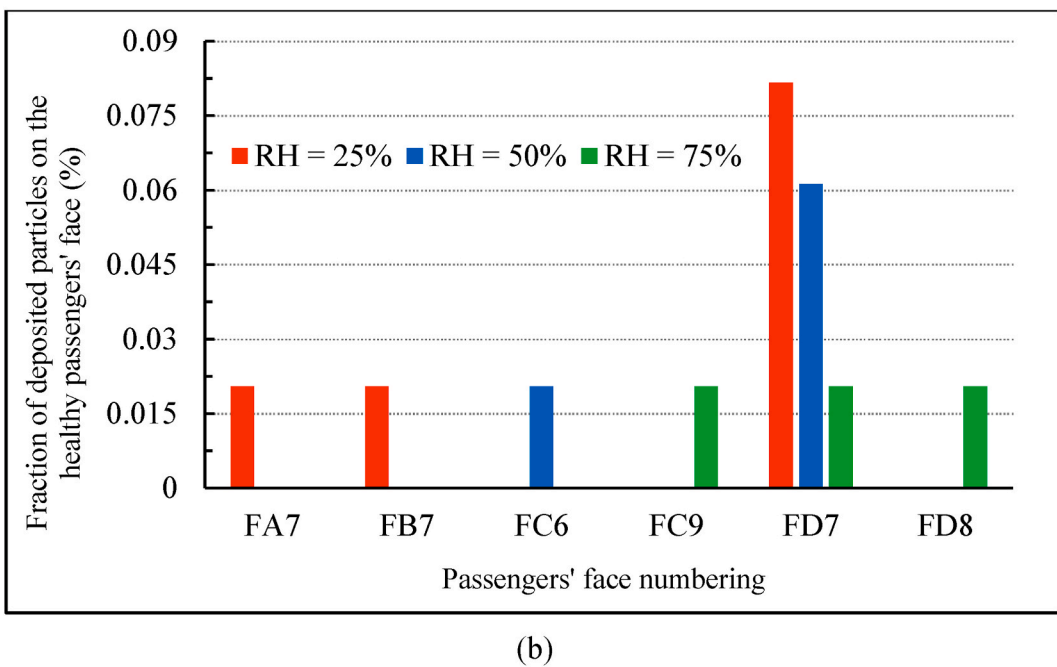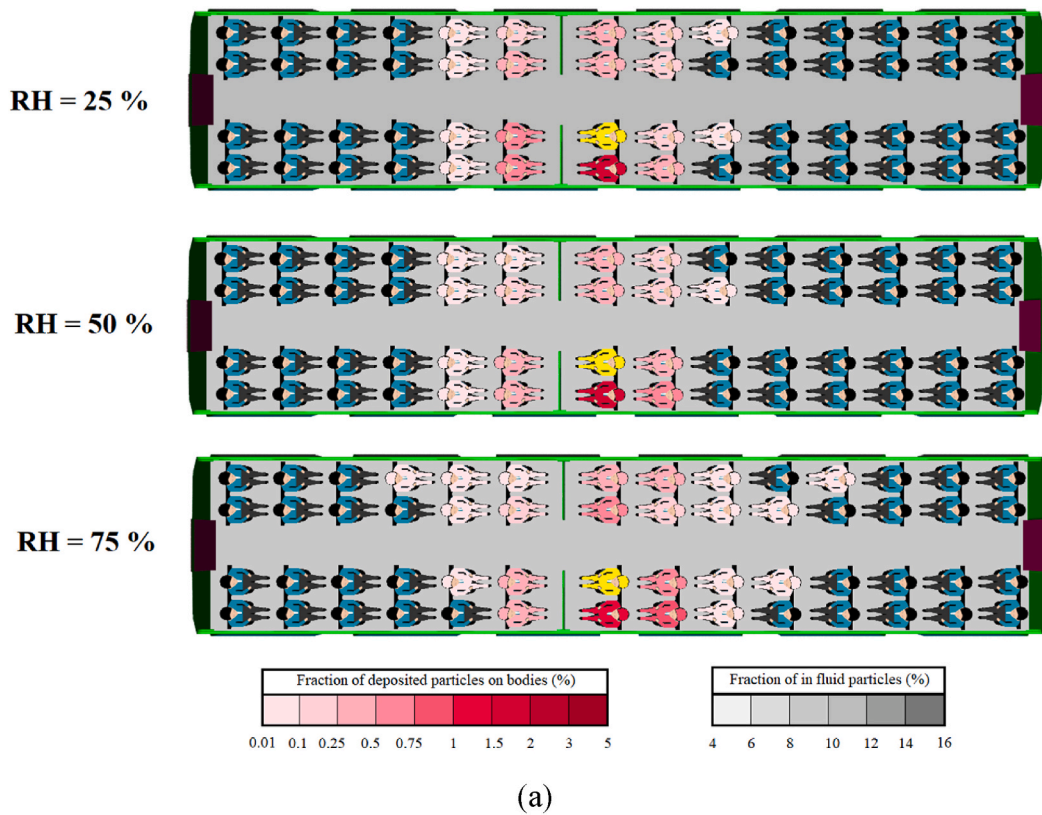
(a)

(b)

Fig. 20. Infection risk analysis for relative humidity. (a) Contours of fraction deposited particles on healthy passengers' body and suspending particles in air, and (b) fraction of deposited particles on the healthy passengers' face.

4.3. Emission source assessment

The location of the patient is also one of the important parameters for evaluating and adopting preventive measures in indoor environments, especially in public transportation systems. This claim was observed by examining the results related to the fraction of
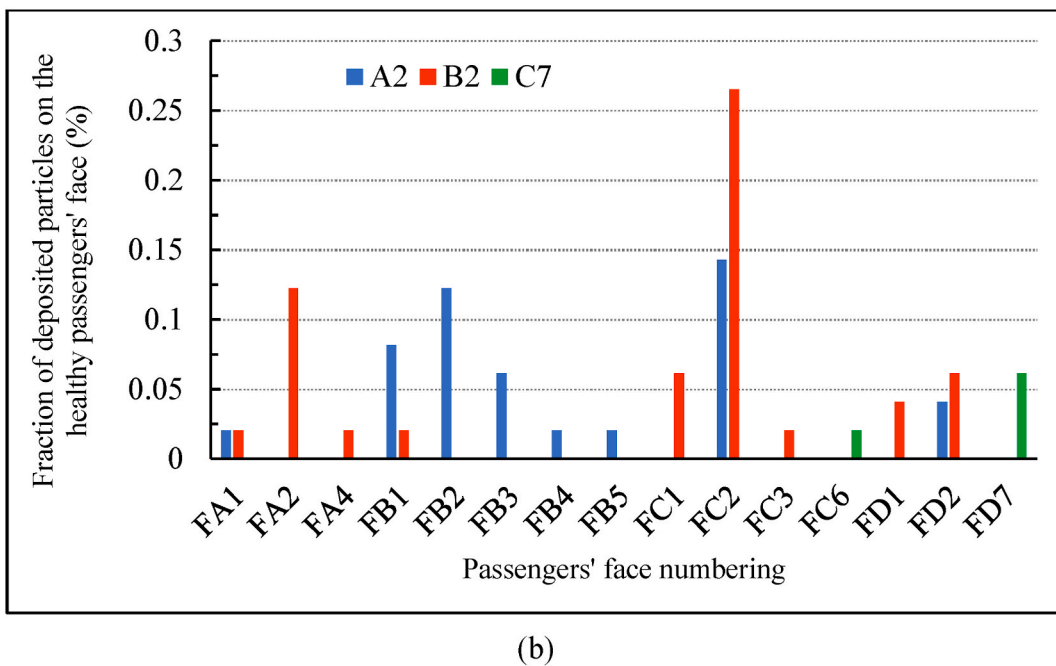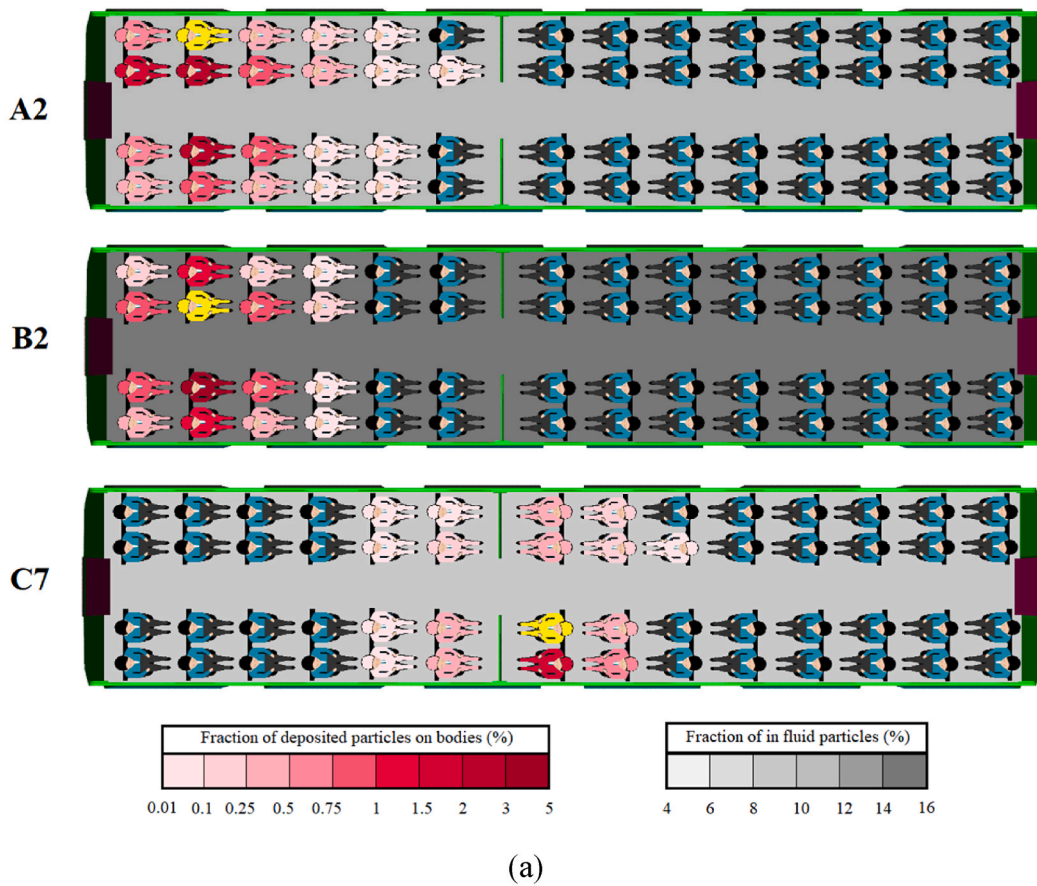
(a)

(b)

Fig. 21. Infection risk analysis for different patient location. (a) Contours of fraction deposited particles on healthy passengers' body and suspending particles in air, and (b) fraction of deposited particles on the healthy passengers' face.

Fig. 22. Infection risk analysis for exhaust's location. (a) Contours of fraction deposited particles on healthy passengers' body and suspending particles in air, and (b) fraction of deposited particles on the healthy passengers' face.
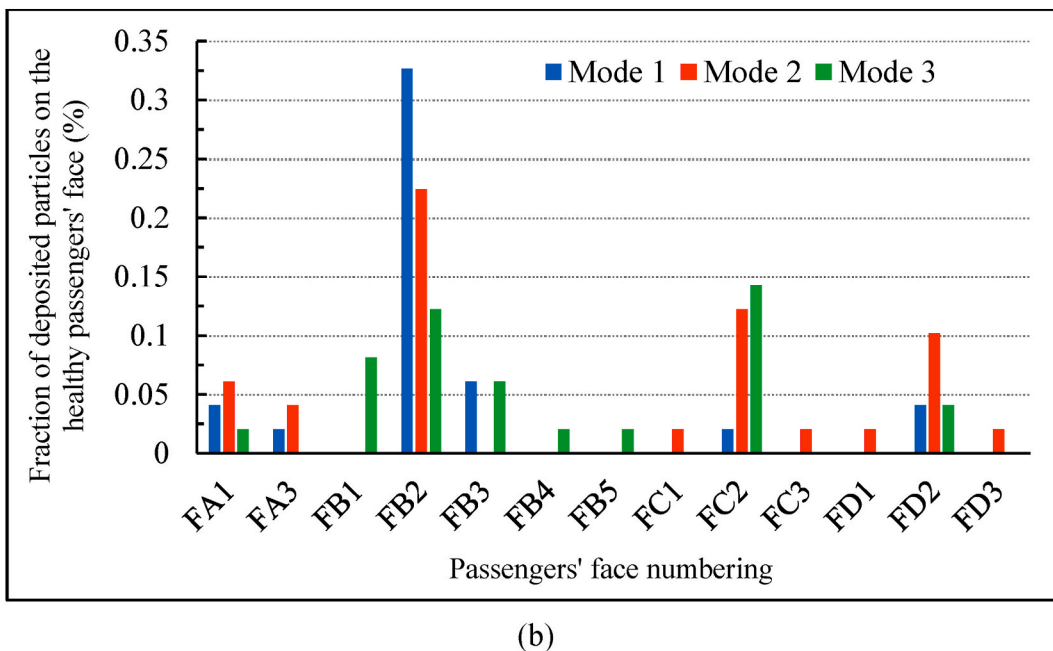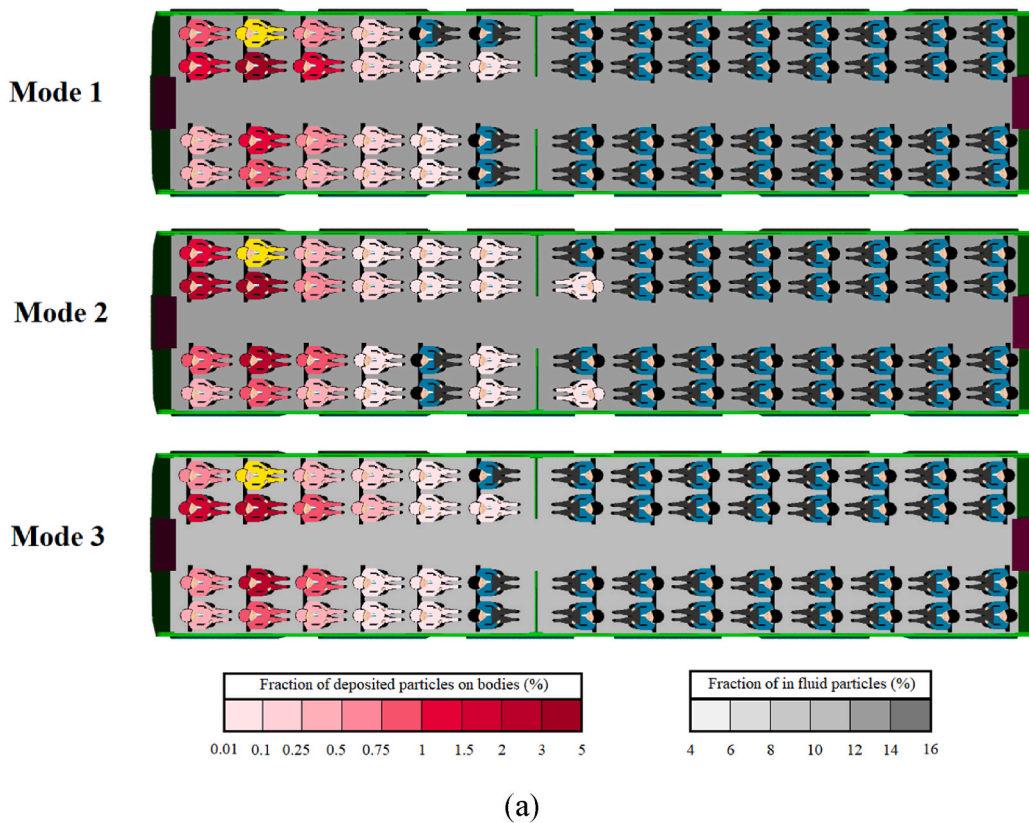
airborne particles and the number of infected people when the emission source is A2 and B2 (Fig. 21). It can be observed that with the movement of the emission source from the adjacency of the window to the middle of the cabin, although the number of people involved has decreased, the air quality is not good and there is still the possibility of other people being contaminated. However, by placing the
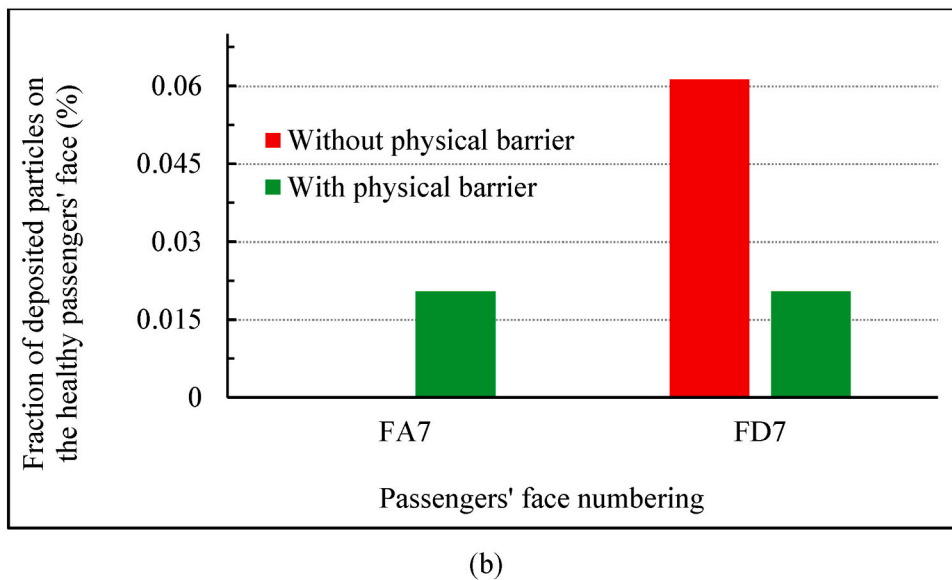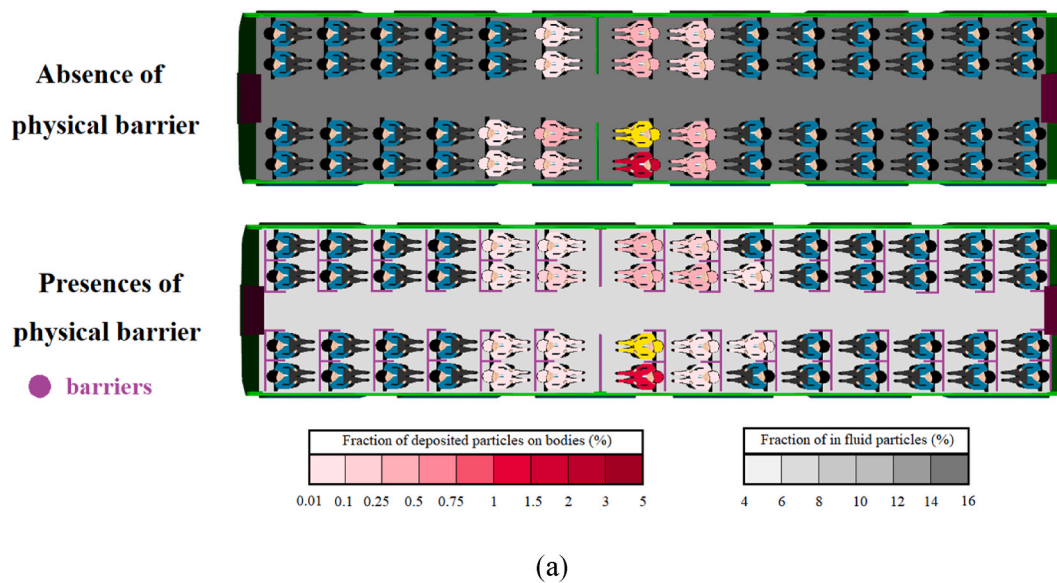
Fig. 23. Infection risk analysis for different patient location. (a) Contours of fraction deposited particles on healthy passengers' body and suspending particles in air, and (b) fraction of deposited particles on the healthy passengers' face.

patient in position C7, the condition of other people will be greatly improved. To better assess the emission source effects on the dispersion of the particles on three different computational planes, including XY, XZ, and YZ planes are presented in supplementary data videos (V1 to V9).

4.4. Exhaust's location assessment

Fig. 22 indicates the effects of the exhaust's location and capacity on the fraction of particles deposited on the body and face of passengers. Passengers sitting in the back row, front and side of the infected passenger face the highest risk. As can be seen, increasing the exhaust capacity not only increases the severity of the involvement of people (fractional deposited particles on the face), but also increases the penetration length of particles inside the cabin. Therefore, it can be depicted that increasing the exhaust capacity in addition to improving the air quality inside the cabin in terms of suspended particles, by reducing the fraction of particles deposition on the face of healthy individuals can also play an important role in reducing the risk of infection in healthy people.

4.5. Physical barriers assessment

Creating physical barriers within public transport systems between seats, especially around the occupants' heads, in addition to protecting their privacy, is also a very low-cost, health-oriented way to prevent the spread of pathogens factors, such as COVID-19
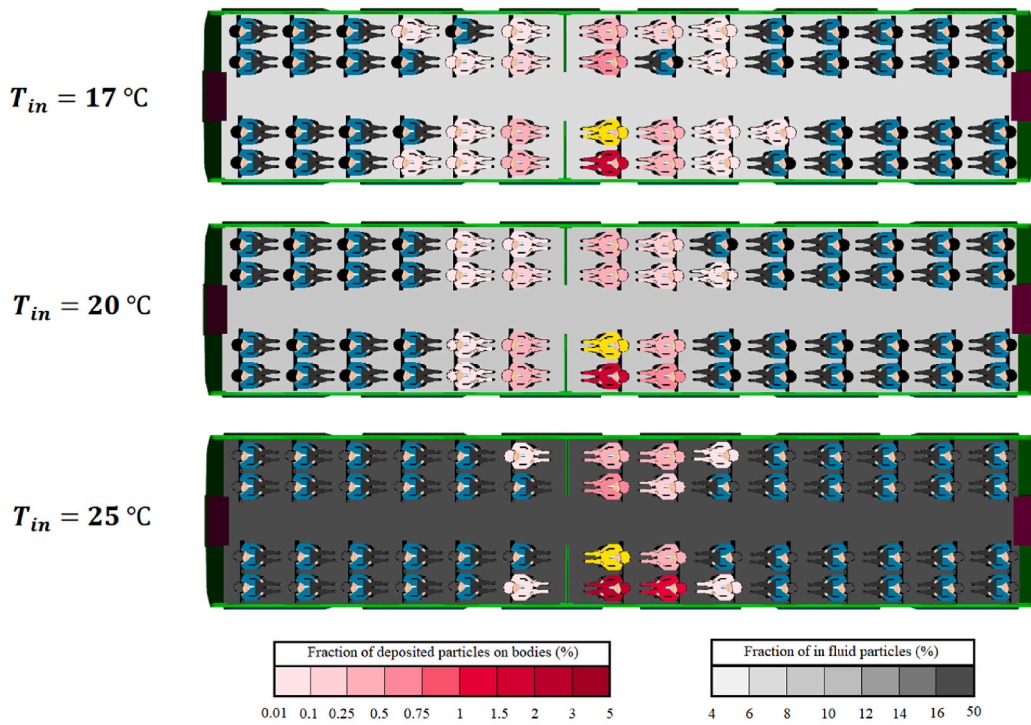
(a)
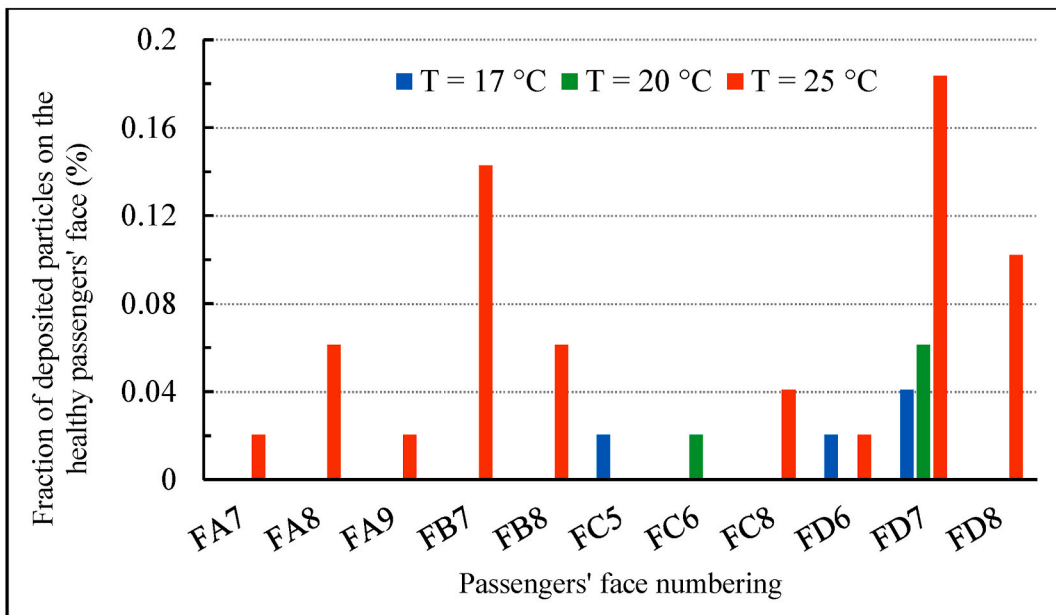
(b)

Fig. 24. Infection risk analysis for different input airflow temperatures. (a) Contours of fraction deposited particles on healthy passengers' body and suspending particles in air, and (b) fraction of deposited particles on the healthy passengers' face.

disease. Fig. 23 shows the effect and importance of the physical barriers. Since the created physical barriers improve cabin air quality in a short time, the following comparison has performed in 160 s. Although at first glance it seems that in the absence of physical barriers, people are less contaminated, this observation can be deceptive. Because it should be noted that the fraction of airborne particles (in short, cabin air quality) in this case is in the worst condition compared to the presence of physical barriers (15% vs. 6%). And this shows that over time, more people are likely to become infected during this scenario. Furthermore, to better assess a comparison of the aerosol-cloud profiles between the presence and absence of the physical barrier over time on three different computational planes, including XY, XZ, and YZ planes are presented in Fig. C3 to C6 (Appendix C).

4.6. Temperature assessment

In another assessment, Fig. 24 shows passengers who are at high risk of infection due to variations of ambient temperature. Fig. 24 (a) examinations indicate that under warmer conditions, people are less at risk. However, at the end of the simulation, more than a third of the injected droplets, are still suspended in the air. Therefore, it cannot be said with certainty that raising the ambient temperature to 25 °C reduces the individuals' infection risk. This conclusion is clearly understood from Fig. 24(b). As can be seen, the number of people the particles are deposited directly on their faces at 25 °C is higher than the other two temperatures. This is while the temperature of 20° is more favorable.

5. Conclusion

In this study, the transmission of aerosols in a common long high-speed train cabin (LHSTC) is studied numerically for different scenarios. The Eulerian-Lagrangian model was employed to assess the dispersion of cough droplets, accounting for the effects of non-volatile components on droplet evaporation. The effects of ventilation rate, relative humidity, injection source, location and capacity of exhausts, and temperature on evaporation and transport of respiratory droplets are investigated. In addition, a powerful tool was introduced to reduce the risk of infection by creating physical barriers around the head and above the passenger seats. The data produced from these simulations may be used to improve policies regarding procedures during outbreaks of human contagions or pandemics. Several conclusions may be drawn from the data presented in this study, as follows:

1. The results implying that the critical role of supply velocity on dispersion and residence time of the droplets. So that, by doubling the rate of inlet ventilation, the fraction of suspended particles (or particle shelf life) reduces by more than 2.8 times, and the fraction of escaped particles increases by more than 7 times, while tripling the ventilation rate can enhance these values to above 3.5 and 9.5 times, respectively.
2. At high RH the final water content of the droplets is greater. And increasing the RH, in addition to raising the time required for the droplets to evaporate, accelerates the process of particles leaving the environment and reduces the fraction of suspended particles.
3. Due to the significant differences between the created recirculation zones (in terms of strength and area), as well as the characteristics of the local airflow, investigating the role of the droplets emission location in indoor environments is a necessary parameter. The results reveal that patient location plays a significant role in the infection risk of healthy individuals.
4. Regarding that most of the droplets evaporate as soon as they are released, this leads to moved towards the exhaust by airflow, and as a result, as the exhaust capacity increases, the particle exit also increases.
5. The presence of physical barriers strongly affects the shelf life of particles. In such a way that after about 1 min of simulation time, the fraction of suspended particles in presence of physical barriers shows a reduction of more than 50% compared to the case where there are no barriers.

Our findings suggest that creating physical barriers, increasing ventilation rates, selecting medium relative humidity, and increasing exhaust capacity can be healthy and cost-effective solutions to viral diseases such as COVID-19.

Author contribution statement

Mahdi Ahmadzadeh: Conceptualization; Data curation; Formal analysis; Investigation; Methodology; Revision; Simulation; Software; Validation; Visualization; Writing-Original Draft. **Mehrzad Shams:** Conceptualization; Writing-Review & Editing; Supervision.

Declaration of competing interest

The authors declare that they have no known competing financial interests or personal relationships that could have appeared to influence the work reported in this paper.

Appendix A. Supplementary data

Supplementary data to this article can be found online at https://doi.org/10.1016/j.jobe.2022.104544.

References

[1] A. Sharma, S. Tiwari, M.K. Deb, J.L. Marty, Severe acute respiratory syndrome coronavirus-2 (SARS-CoV-2): a global pandemic and treatment strategies, Int. J. Antimicrob. Agents 56 (2) (Aug. 2020), 106054, https://doi.org/10.1016/j.ijantimicag.2020.106054.

[2] WHO, "Global research on coronavirus disease (COVID-19), WHO Databse, 2021, pp. 2019–2022 [Online]. Available: https://www.who.int/emergencies/diseases/novel-coronavirus-2019/global-research-on-novel-coronavirus-2019-ncov.

[3] J.S. Kutter, et al., SARS-CoV and SARS-CoV-2 are transmitted through the air between ferrets over more than one meter distance, Nat. Commun. 12 (1) (2021), https://doi.org/10.1038/s41467-021-21918-6.

[4] Y. Liu, et al., Viral dynamics in mild and severe cases of COVID-19, Lancet Infect. Dis. 20 (6) (2020) 656–657, https://doi.org/10.1016/S1473-3099(20)30232-2.

[5] G.A. Somsen, C. van Rijn, S. Kooij, R.A. Bem, D. Bonn, Small droplet aerosols in poorly ventilated spaces and SARS-CoV-2 transmission, Lancet Respir. Med. 8 (7) (2020) 658–659, https://doi.org/10.1016/S2213-2600(20)30245-9.

[6] C.C. Wang, et al., Airborne transmission of respiratory viruses, Science 373 (6558) (2021), https://doi.org/10.1126/science.abd9149.

[8] M. Arslan, B. Xu, M. Gamal El-Din, Transmission of SARS-CoV-2 via fecal-oral and aerosols–borne routes: environmental dynamics and implications for wastewater management in underprivileged societies, Sci. Total Environ. 743 (2020), 140709, https://doi.org/10.1016/j.scitotenv.2020.140709.

[9] Zhai, Evaluation of various turbulence models in predicting airflow and turbulence in enclosed environments by CFD: Part-1, Ashrae 13 (6) (2012) 1–26.

[10] Z.J. Zhai, Z. Zhang, W. Zhang, Q.Y. Chen, Evaluation of various turbulence models in predicting airflow and turbulence in enclosed environments by CFD: Part 1—summary of prevalent turbulence models, HVAC R Res. 13 (6) (2007) 853–870.

[11] F. Mohamadi, A. Fazeli, A review on applications of CFD modeling in COVID-19 pandemic, no. December, Arch. Comput. Methods Eng. (2021), https://doi.org/10.1007/s11831-021-09706-3, 2022.

[12] G.M. Thornton, et al., The impact of heating, ventilation, and air conditioning design features on the transmission of viruses, including the 2019 novel coronavirus: a systematic review of ultraviolet radiation, PLoS One 17 (4) (Apr. 2022), e0266487, https://doi.org/10.1371/journal.pone.0266487 [Online]. Available:.

[13] M. Ahmadzadeh, E. Farokhi, M. Shams, Investigating the effect of air conditioning on the distribution and transmission of COVID-19 virus particles, J. Clean. Prod. 316 (2021), 128147, https://doi.org/10.1016/j.jclepro.2021.128147.

[14] M. Mirzaie, E. Lakzian, A. Khan, M.E. Warkiani, O. Mahian, G. Ahmadi, COVID-19 spread in a classroom equipped with partition – a CFD approach, J. Hazard. Mater. 420 (2021), 126587, https://doi.org/10.1016/j.jhazmat.2021.126587.

[15] C. Shum, Y. Alipouri, L. Zhong, Examination of human interaction on indoor environmental quality variables: a case study of libraries at the University of Alberta, Build. Environ. 207 (PB) (2022), 108476, https://doi.org/10.1016/j.buildenv.2021.108476.

[16] M. Ahmadzadeh, M. Shams, Passenger exposure to respiratory aerosols in a train cabin: effects of window, injection source, output flow location, Sustain. Cities Soc. 75 (Dec. 2021), 103280, https://doi.org/10.1016/j.SCS.2021.103280.

[17] A. Nazari, M. Jafari, N. Rezaei, F. Taghizadeh-Hesary, F. Taghizadeh-Hesary, Jet fans in the underground car parking areas and virus transmission, Phys. Fluids 33 (1) (2021), https://doi.org/10.1063/5.0033557.

[18] A. Nazari, Reducing Virus Transmission From Heating , Ventilation , and Air Conditioning Systems of Urban Subways, 2021, 0–36.

[19] K. Talaat, M. Abuhegazy, O.A. Mahfoze, O. Anderoglu, S.V. Poroseva, Simulation of aerosol transmission on a Boeing 737 airplane with intervention measures for COVID-19 mitigation, Phys. Fluids 33 (3) (2021) 1–13, https://doi.org/10.1063/5.0044720.

[20] C. Crawford, et al., Modeling of aerosol transmission of airborne pathogens in ICU rooms of COVID-19 patients with acute respiratory failure, Sci. Rep. 11 (1) (2021) 1–12, https://doi.org/10.1038/s41598-021-91265-5.

[21] V.G. Melnikova, A.S. Epikhin, M.V. Kraposhin, The eulerian–Lagrangian approach for the numerical investigation of an acoustic field generated by a high-speed gas-droplet flow, Fluids 6 (8) (2021), https://doi.org/10.3390/fluids6080274.

[22] G. Hu, I. Celik, Eulerian-Lagrangian based large-eddy simulation of a partially aerated flat bubble column, Chem. Eng. Sci. 63 (1) (2008) 253–271, https://doi.org/10.1016/j.ces.2007.09.015.

[23] E.A. Hathway, C.J. Noakes, P.A. Sleigh, L.A. Fletcher, CFD simulation of airborne pathogen transport due to human activities, Build. Environ. 46 (12) (2011) 2500–2511, https://doi.org/10.1016/j.buildenv.2011.06.001.

[24] Z. Zhang, Q. Chen, Comparison of the Eulerian and Lagrangian methods for predicting particle transport in enclosed spaces, Atmos. Environ. 41 (25) (2007) 5236–5248, https://doi.org/10.1016/j.atmosenv.2006.05.086.

[25] V. Mathai, A. Das, J.A. Bailey, K. Breuer, Airflows inside passenger cars and implications for airborne disease transmission, Sci. Adv. 7 (1) (2021) 1–7, https://doi.org/10.1126/sciadv.abe0166.

[26] Z. Zhang, T. Han, K.H. Yoo, J. Capecelatro, A.L. Boehman, K. Maki, Disease transmission through expiratory aerosols on an urban bus, Phys. Fluids 33 (1) (2021), https://doi.org/10.1063/5.0037452.

[27] J. Wang, G. Du, COVID-19 may transmit through aerosol, Ir. J. Med. Sci. 189 (4) (2020) 1143–1144, https://doi.org/10.1007/s11845-020-02218-2.

[28] V. D'Alessandro, M. Falone, L. Giammichele, R. Ricci, Eulerian-Lagrangian modeling of cough droplets irradiated by ultraviolet-C light in relation to SARS-CoV-2 transmission, Phys. Fluids 33 (3) (2021), https://doi.org/10.1063/5.0039224.

[29] I.T.S. Yu, et al., Evidence of airborne transmission of the severe acute respiratory syndrome virus, N. Engl. J. Med. 350 (17) (Apr. 2004) 1731–1739, https://doi.org/10.1056/NEJMoa032867.

[30] J. Gralton, E.R. Tovey, M.L. Mclaws, W.D. Rawlinson, Respiratory virus RNA is detectable in airborne and droplet particles, J. Med. Virol. 85 (12) (2013) 2151–2159, https://doi.org/10.1002/jmv.23698.

[31] T. Zhang, Q. Wu, Z. Zhang, Probable pangolin origin of SARS-CoV-2 associated with the COVID-19 outbreak, Curr. Biol. 30 (7) (2020) 1346–1351, https://doi.org/10.1016/j.cub.2020.03.022, e2.

[32] A.L. Katelaris, et al., Epidemiologic evidence for airborne transmission of SARS-CoV-2 during Church singing, Australia, Emerg. Infect. Dis. 27 (6) (2020) 1677–1680, https://doi.org/10.3201/eid2706.210465, 2021.

[33] A.A. Rabaan, et al., Airborne transmission of SARS-CoV-2 is the dominant route of transmission: droplets and aerosols, Le Infez. Med. 29 (1) (Mar. 2021) 10–19.

[34] B. Li, et al., Experimental studies of thermal environment and contaminant transport in a commercial aircraft cabin with gaspers on, Indoor Air 26 (5) (2016) 806–819, https://doi.org/10.1111/ina.12265.

[35] C.Y.H. Chao, et al., Characterization of expiration air jets and droplet size distributions immediately at the mouth opening, J. Aerosol Sci. 40 (2) (Feb. 2009) 122–133, https://doi.org/10.1016/j.jaerosci.2008.10.003.

[36] J.K. Gupta, C.-H. Lin, Q. Chen, Characterizing exhaled airflow from breathing and talking, Indoor Air 20 (1) (Feb. 2010) 31–39, https://doi.org/10.1111/j.1600-0668.2009.00623.x.

[37] J.K. Gupta, C.H. Lin, Q. Chen, Flow dynamics and characterization of a cough, Indoor Air 19 (6) (2009) 517–525, https://doi.org/10.1111/j.1600-0668.2009.00619.x.

[38] J.P. Duguid, The size and the duration of air-carriage of respiratory droplets and droplet-nuclei, J. Hyg. 44 (6) (Sep. 1946) 471–479, https://doi.org/10.1017/s0022172400019288.

[39] L. Liu, J. Wei, Y. Li, A. Ooi, Evaporation and dispersion of respiratory droplets from coughing, Indoor Air 27 (1) (2017) 179–190, https://doi.org/10.1111/ina.12297.

[40] J.W. Tang, Y. Li, I. Eames, P.K.S. Chan, G.L. Ridgway, Factors involved in the aerosol transmission of infection and control of ventilation in healthcare premises, J. Hosp. Infect. 64 (2) (2006) 100–114, https://doi.org/10.1016/j.jhin.2006.05.022.

[41] T. Dbouk, D. Drikakis, Weather impact on airborne coronavirus survival, Phys. Fluids 32 (9) (2020), https://doi.org/10.1063/5.0024272.

[42] P. Mecenas, R.T. da Rosa Moreira Bastos, A.C. Rosário Vallinoto, D. Normando, Effects of temperature and humidity on the spread of COVID-19: a systematic review, PLoS One 15 (9 September) (2020) 1–21, https://doi.org/10.1371/journal.pone.0238339.

[43] I. Jacob, D. Journals, Pr Ep Rin T N Ot Pe Er R Iew Pr Ep Rin T N Ot Pe Er R, vol. 7, June, 2014, pp. 285–292.

[44] E.P. Vejerano, L.C. Marr, Physico-chemical characteristics of evaporating respiratory fluid droplets, J. R. Soc. Interface 15 (139) (2018) 1–10, https://doi.org/10.1098/rsif.2017.0939.

[45] K.K.W. To, et al., Consistent detection of 2019 novel coronavirus in saliva, Clin. Infect. Dis. 71 (15) (2020) 841–843, https://doi.org/10.1093/cid/ciaa149.

[46] H. Wang, M. Lin, Y. Chen, Performance evaluation of air distribution systems in three different China railway high-speed train cabins using numerical simulation, Build. Simulat. 7 (6) (2014) 629–638, https://doi.org/10.1007/s12273-014-0168-5.

[47] L. Yang, M. Li, X. Li, J. Tu, The effects of diffuser type on thermal flow and contaminant transport in high-speed train (HST) cabins–a numerical study, Int. J. Vent. 17 (1) (2018) 48–62, https://doi.org/10.1080/14733315.2017.1351736.

[48] H.S. Jang, J.H. Kim, J.Y. Jeon, Evaluation of speech privacy on the seat-design in high-speed train passenger cars, Trans. Korean Soc. Noise Vib. Eng. 24 (2) (2014) 146–153, https://doi.org/10.5050/ksnve.2013.24.2.146.

[49] H.S. Jang, H. Lim, J.Y. Jeon, Control of interior surface materials for speech privacy in high-speed train cabins, Indoor Air 27 (3) (2017) 670–679, https://doi.org/10.1111/ina.12339.

[50] L. Zhang, Y. Li, Dispersion of coughed droplets in a fully-occupied high-speed rail cabin, Build. Environ. 47 (1) (2012) 58–66, https://doi.org/10.1016/j.buildenv.2011.03.015.

[51] L. Zhang, 张磊, Dispersion of Coughed Droplets in Crowded Indoor Environment, The University of Hong Kong (Pokfulam, Hong Kong), 2011.

[52] W.G. Lindsley, et al., Quantity and size distribution of cough-generated aerosol particles produced by influenza patients during and after illness, J. Occup. Environ. Hyg. 9 (7) (2012) 443–449, https://doi.org/10.1080/15459624.2012.684582.

[53] S. Khatoon, M.H. Kim, Thermal comfort in the passenger compartment using a 3-D numerical analysis and comparison with Fanger's comfort models, Energies 13 (3) (2020), https://doi.org/10.3390/en13030690.

[54] M. Mahdavimanesh, M. Behbahaninejad, G. Ahmadi, M. Dehghanian, Lagrangian Particle Tracking, Model Development, 2013.

[55] C. Chen, B. Zhao, Some questions on dispersion of human exhaled droplets in ventilation room: answers from numerical investigation, Indoor Air 20 (2) (2010) 95–111, https://doi.org/10.1111/j.1600-0668.2009.00626.x.

[56] A. Li, G. Ahmadi, Dispersion and deposition of spherical particles from point sources in a turbulent channel flow, Aerosol Sci. Technol. 16 (4) (1992) 209–226, https://doi.org/10.1080/02786829208959550.

[57] D. Hryb, M. Cardozo, S. Ferro, M. Goldschmit, Particle transport in turbulent flow using both Lagrangian and Eulerian formulations, Int. Commun. Heat Mass Tran. 36 (5) (2009) 451–457, https://doi.org/10.1016/j.icheatmasstransfer.2009.01.017.

[58] B.N. Bailey, Numerical considerations for Lagrangian stochastic dispersion models: eliminating rogue trajectories, and the importance of numerical accuracy, Boundary-Layer Meteorol. 162 (1) (2017) 43–70, https://doi.org/10.1007/s10546-016-0181-6.

[59] A.D. Gosman, E. Ioannides, Aspects of computer simulation of liquid-fuelled combustors, AIAA Pap. 7 (6) (1981) 482–490, https://doi.org/10.2514/6.1981-323.

[60] R.L. Hedrick, et al., Ventilation for acceptable indoor air quality, ASHRAE Stand. 2013 (62.1) (2013), 2013, [Online]. Available: www.ashrae.org.

[61] S.W. Zhu, S. Kato, J.H. Yang, Study on transport characteristics of saliva droplets produced by coughing in a calm indoor environment, Build. Environ. 41 (12) (2006) 1691–1702, https://doi.org/10.1016/j.buildenv.2005.06.024.

[62] X. Li, Y. Shang, Y. Yan, L. Yang, J. Tu, Modelling of evaporation of cough droplets in inhomogeneous humidity fields using the multi-component Eulerian-Lagrangian approach, Build. Environ. 128 (July 2017) 68–76, https://doi.org/10.1016/j.buildenv.2017.11.025, 2018.

[63] S. Shao, et al., Risk assessment of airborne transmission of COVID-19 by asymptomatic individuals under different practical settings, J. Aerosol Sci. 151 (2021), 105661, https://doi.org/10.1016/j.jaerosci.2020.105661.

[64] Z. Dong, B. Zhou, F. Li, Y. Wang, X. Lin, X. Wu, ScienceDirect ScienceDirect investigation of thermal plume around a simulated standing operator in an operating room, Procedia Eng. 205 (2017) 1940–1945, https://doi.org/10.1016/j.proeng.2017.10.053.

[65] S. Sun, J. Li, J. Han, How human thermal plume influences near - human transport of respiratory droplets and airborne particles : a review, Environ. Chem. Lett. 19 (3) (2021) 1971–1982, https://doi.org/10.1007/s10311-020-01178-4.